





REVIEW ARTICLE

Open Access

Recent progress with one-dimensional metal halide perovskites: from rational synthesis to optoelectronic applications

Dawei Duan¹, Chuangye Ge¹, Md Zahidur Rahaman², Chun-Ho Lin¹, Yumeng Shi³, Haoran Lin¹, Hanlin Hu¹ and Tom Wu^{1,2,4}

Abstract

Metal halide perovskites can be readily synthesized, they exhibit tunable physical properties and excellent performance, and they are heavily studied optoelectronic materials. Compared to the typical three-dimensional perovskites, morphological-level one-dimensional (1D) nanostructures enable charge transport and photon propagation with low exciton binding energies and long charge-carrier diffusion lengths, while molecular-level 1D nanostructures exhibit good compositional and structural flexibilities, highly tunable bandgaps, strong quantum confinement effects, and excellent ambient stabilities. The 1D natures of these emerging halide perovskites enhance the performance of optoelectronic devices. Herein, we highlight recent progress realized in the syntheses and characterizations of both morphological- and molecular-level 1D halide perovskites with tunable structures, compositions, and properties, as well as their photovoltaic, light-emission, and photodetection applications. In addition, current challenges, future prospects, and promising research directions are discussed to provide guidance in advancing the field of 1D perovskites.

Introduction

The dimensionality of a semiconducting material plays a significant role in the structure, properties, and performance of the corresponding device as well. In a particular semiconductor, the dimensionality induces completely different light-matter and electronic interactions. Significant advancements have been realized in the development and application of low-dimensional semiconductors, such as elemental, compound, and metal chalcogenide semiconductors¹. One of the major motivations behind these efforts has been to investigate the relationships among the properties and performance of

these semiconducting materials by regulating their dimensionality, structure, and composition. Substantial effort has also been devoted to revealing how the dimensionality affects these materials in order to develop cost-effective, efficient and stable devices^{2–4}.

Metal halide perovskites (MHPs) are highly sought-after semiconducting materials for optoelectronics. The general formula of three-dimensional (3D) MHPs is ABX_3 , where the A-site contains a cation, including $CH_3NH_3^+$, $CH(NH_2)_2^+$, and Cs^+ ; B-site contains a metal cation, such as Pb^{2+} and other ions such as Sn^{2+} , Bi^{3+} , and Cu^{2+} ; and the X-sites contain halide anions, which might be I^- , Br^- or Cl^- ^{5–10}. In terms of the dimensionality of MHPs, there are four categories: zero-dimensional (0D), one-dimensional (1D), two-dimensional (2D), and 3D, depending on the spatial arrangements of the octahedral units^{11–13}. 3D MHPs display many unique characteristics, including solution processability, and superior device performance since Kojima et al. introduced them as

Correspondence: Hanlin Hu (hanlinhu@szpt.edu.cn) or Tom Wu (tom.wu@unsw.edu.au)

¹Hoffmann Institute of Advanced Materials, Postdoctoral Innovation Practice Base, Shenzhen Polytechnic, Nanshan District, Shenzhen 518055, P. R. China

²School of Materials Science and Engineering, University of New South Wales (UNSW), Sydney, NSW 2052, Australia

Full list of author information is available at the end of the article

These authors contributed equally: Dawei Duan, Chuangye Ge.

© The Author(s) 2023



Open Access This article is licensed under a Creative Commons Attribution 4.0 International License, which permits use, sharing, adaptation, distribution and reproduction in any medium or format, as long as you give appropriate credit to the original author(s) and the source, provide a link to the Creative Commons license, and indicate if changes were made. The images or other third party material in this article are included in the article's Creative Commons license, unless indicated otherwise in a credit line to the material. If material is not included in the article's Creative Commons license and your intended use is not permitted by statutory regulation or exceeds the permitted use, you will need to obtain permission directly from the copyright holder. To view a copy of this license, visit <http://creativecommons.org/licenses/by/4.0/>.

sensitizers of liquid dye-sensitized solar cells (DSSCs) with a power conversion efficiencies (PCE) of 3.8%^{14,15}. Due to the strong optical absorptions, tunable bandgaps, long diffusion lengths and charge carrier lifetimes, high charge-carrier mobilities, and high photoluminescence quantum yields (PLQYs), 3D MHPs have been employed for various applications, such as solar cells^{16,17}, light-emitting diodes (LEDs)^{18,19}, lasers^{20,21}, photodetectors (PDs)^{22,23}, memory devices^{24,25}, and field-effect transistors (FETs)²⁶. However, most 3D MHPs are not stable when exposed to ultraviolet (UV) light, oxygen, moisture, or heating, which leading to structural decomposition and significant decay of the performance^{27,28}.

Low-dimensional MHPs, including quasi-2D, 2D, 1D, and 0D versions with controlled morphology and structures, have emerged as environmentally stable materials due to their hydrophobic characteristics and the high binding energy of the excitons^{11,29–31}. Compared to 3D MHPs, low-dimensional MHPs have at least one reduced dimension. This often causes confusion when using the terminology “low dimensional” in different practical situations. To avoid this confusion, we distinguish low-dimensional MHPs according to their final morphologies and crystal structural dimensionalities^{8,12,32}. Morphological level low-dimensional MHPs refer to 0D nanocrystals, 1D nanowires (NWs) or nanorods (NRs), and 2D nanosheets/nanoplatelets, most of which are constructed from a 3D network of $[BX_6]^{4-}$ octahedral units, just as in bulk 3D ABX_3 MHPs^{5,33}. In contrast, molecular-level low-dimensional MHPs emphasize the crystal structures, which means that the individual building blocks of the MHPs display a low-dimensional arrangement at the molecular level. In detail, these $[BX_6]^{4-}$ octahedra often exhibit different forms, such as discrete octahedra (0D), octahedral chains (1D), and octahedral platelets (2D)^{32,34}.

Research on 2D and 0D MHPs has been extensively discussed in the literature^{35–37}. However, there has been no comprehensive review of the crystal and electronic structures of 1D MHPs, both morphological and molecular, to provide insights into their syntheses, properties, and optoelectronic applications. It is crucial to define “molecular-level 1D” and “morphological-level 1D”. Perovskite NWs or NRs may be identified as morphological 1D MHPs with diameters of several up to hundreds of nanometers. They still possess a 3D framework comprising corner-sharing metal halide octahedra and intrinsic properties similar to those of 3D ABX_3 MHPs except for the quantum confinement effect¹¹. In contrast, there are many molecular 1D MHPs in which the anionic metal halide chains are separated by the organic cations in their structures. Their band structures are dictated by the connectivity between the building components. Without size limitations, bulky 1D molecular crystals exhibit optical properties similar to those of single quantum

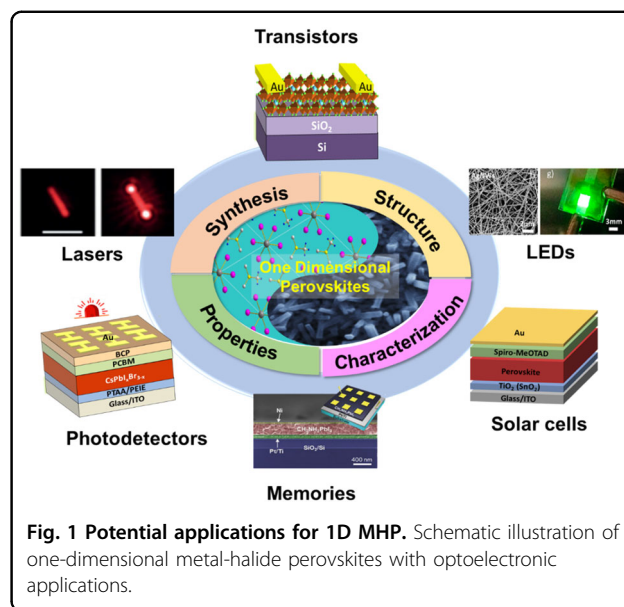


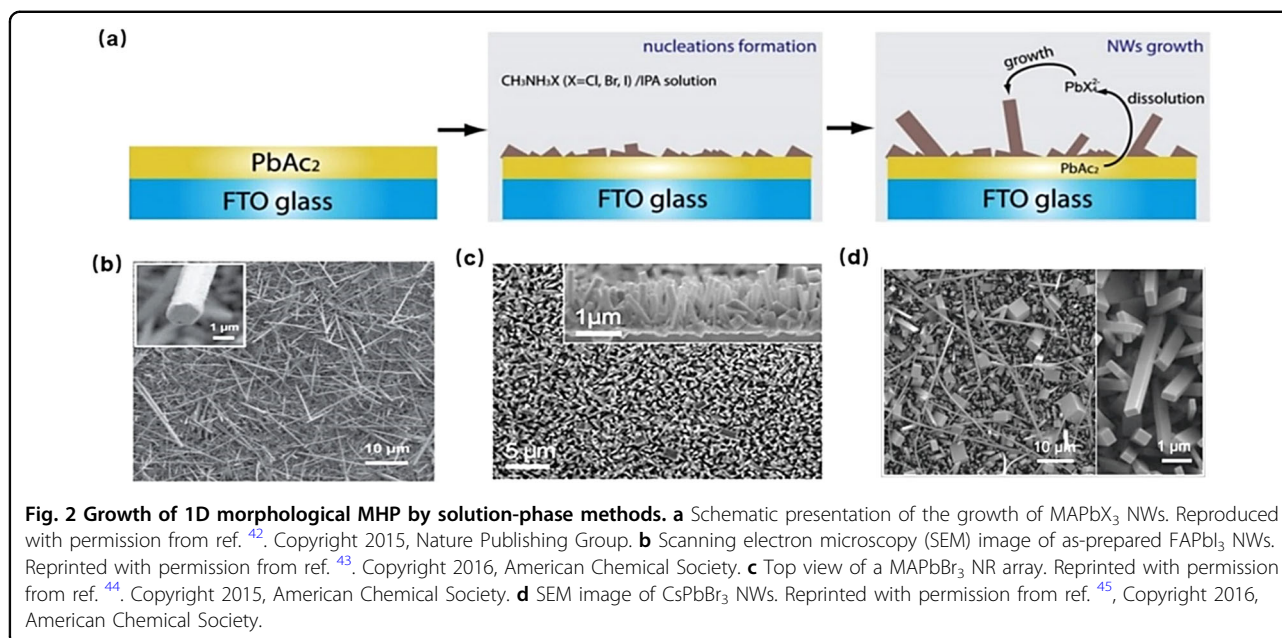
Fig. 1 Potential applications for 1D MHP. Schematic illustration of one-dimensional metal-halide perovskites with optoelectronic applications.

wires⁷. Critically speaking, most molecular 1D MHPs should be called “perovskitoids” because they do not have cubic crystal structures containing corner-shared metal octahedra.

In this review, we focus on the present status of research on both kinds of 1D MHPs in terms of the syntheses, structures, characterization data, and tunable properties originating from their morphological or molecular diversities (as shown in Fig. 1). Furthermore, we summarize various optoelectronic applications based on 1D MHPs with enhanced device performance enabled by their properties. In addition, to offer insight on possible research directions, the current challenges and future prospects of 1D MHPs are also discussed.

Morphological-level one-dimensional MHPs

One dimensional nanostructured MHPs, such as NWs and NRs with diameters of 1–100 nm and lengths of several hundred nanometers or even micrometers, have been applied in many photonic and optoelectronic devices because of their outstanding intrinsic properties, such as long charge-carrier diffusion lengths and lifetimes, large surface-to-volume ratios, and greater charge confinement and anisotropic geometries compared with 3D MHPs^{10,28}. Specifically, Stranks et al. reported that the charge diffusion lengths were ~ 100 nm for 3D $MAPbI_3$ and over $1 \mu m$ for the mixed halide perovskites ($MAPbI_{3-x}Cl_x$)³⁸. In comparison, carrier diffusion lengths of $21 \mu m$ for single-crystalline $MAPbI_3$ NWs and $41 \pm 3 \mu m$ for high-quality single-crystalline $MAPb(I_{1-x}Br_x)_3$ NW arrays were reported^{39,40}. The larger diffusion lengths of the 1D MHPs are associated with much longer lifetimes of the charge carriers and consequently lead to superior devices for optoelectronic applications. In this section, we will



give a brief overview of recent developments in the syntheses and characterizations of 1D MHPs with tunable dimensionality, morphology and compositions. We will also investigate the advantageous physical and chemical properties, improved stability, and applications of the 1D MHPs used in optoelectronic devices.

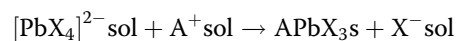
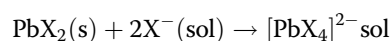
Syntheses of 1D morphological MHPs

Various approaches have been proposed for preparing single-crystalline 1D MHPs, such as solution-phase methods, vapor-phase methods, hot-injection methods, and template-assisted methods. Based on these methods, different applications, such as in solar cells, PDs, LEDs, and lasers, have also been extensively explored.

Solution-phase methods

Low-temperature solution processability is one of the most useful features enabling preparation of high-quality MHP single crystals or thin films on different substrates. This feasible technique offers vast structural and compositionality tunability. In 2014⁴¹, Horváth and coworkers employed a low-temperature solution crystallization approach to prepare MAPbI₃ NWs with a slip-coating process, in which they dripped a saturated MAPbI₃ precursor solution between two glass slides and then moved the upper glass slowly in a particular direction. The solvent of the thin liquid perovskite film evaporated when exposed to the ambient air, leading to the formation of MAPbI₃ NWs showing average diameters of up to 400 nm. Compared with conventional nanoparticles, the as-grown NWs exhibited better charge transport.

In another study by Zhu and coworkers, a two-step method was proposed, in which they first spin-coated PbAc₂ on a glass substrate and then immersed it into a MAX solution (X = Cl, Br, I or a mixture of halides) (Fig. 2)⁴². The rapidly formed MAPbI₃ initiated growth of the NWs but also stopped the reaction between the unreacted PbAc₂ and the MAI. Moreover, slow dissolution of the initial MAPbI₃ layer and the unreacted PbAc₂ occurred and inhibited the generation of [Pb₄]²⁻, which provided supersaturation and promoted growth of the 1D NWs. Screw dislocations facilitated the anisotropic growth of the NWs without a catalyst, which was proven by the spontaneous generation of NWs with flat rectangular end facets. The authors proposed a growth mechanism involving dissolution-recrystallization, in which a soluble intermediate formed at a high concentration of the organic halide salt (AX):^{5,42}



Following this work, a wide range of MHP NWs or NRs with various cations and anions was synthesized. For instance, Fu and coworkers prepared formamidinium (FA)-lead halide perovskite NWs with enhanced thermal stability⁴³. Yang's group fabricated MAPbBr₃ NR arrays at room temperature and converted them to MAPbI₃ by anion exchange with MAI vapor without changing their morphologies⁴⁴.

An anion exchange-based solution synthetic strategy for preparing 1D MHPs was extended to the syntheses of all-inorganic CsPbX₃ (X = Cl, Br, I) MHP NWs⁴⁵.

The obtained NWs exhibited single crystalline natures and smooth end facets with excellent long-term stability under ambient conditions for over a few weeks^{8,13}. The key to successful formation of the high-quality 1D NWs was to select a solvent in which AX is highly soluble and the perovskite products are not, which ensures slow formation of the $[\text{PbX}_4]^{2-}$ intermediate and provides an optimal concentration of AX to maintain the low supersaturation condition^{46,47}.

Vapor phase methods

Compared to solution processes, vapor-phase syntheses are often conducted at higher temperatures, which can produce 1D MHPs with fewer defects and superb crystallinity. Despite the versatility of the solution phase synthetic techniques, they are plagued by the problem of surface contamination. In this respect, vapor phase growth methods have an obvious advantage over solution methods. In 2014, Xiong's group demonstrated a two-step chemical vapor deposition (CVD) synthesis of MAPbCl_3 NWs⁴⁸. In that work, PbCl_2 NWs were grown by a CVD approach and then converted into the MHP NWs by reacting them with vapor-phase MACl molecules. However, the yield was quite low, and high percentages of 2D MHP platelet byproducts were obtained. To enhance the yield of the 1D NWs, they prepared free-standing MAPbX_3 ($X = \text{I}, \text{Br}$, or a mixture of I and Cl) NWs via a two-step vapor-phase synthesis on a silicon oxide substrate⁴⁹. Thermally stable all-inorganic perovskites with tunable properties and improved crystallinity and stability were also produced. In another study reported by Chen et al., CsPbX_3 ($X = \text{Cl}, \text{Br}$, or I) NWs and microwires (MWs) with horizontal orientations on mica were fabricated by vapor-phase epitaxial growth. A mixture of the precursor PbX_2 and CsX powders was placed in a furnace with a temperature between 300 and 350 °C⁵⁰. The evaporated precursor was carried to the downstream region by argon gas, where the substrate was positioned. The NWs displayed triangular cross-sections and tuned crystallographic orientations. The anisotropic growth might be attributed to the asymmetric lattice mismatch, which induced directional growth along the $[001]$ plane. Graphoepitaxy on a faceted sapphire plane guided the growth of CsPbBr_3 NWs with lengths up to millimeters.

High-quality perovskite NRs prepared by vapor growth have rarely been reported. Zhou and coworkers demonstrated the preparation of all-inorganic MHP NRs via vapor phase deposition⁵¹. In their work, a mixture of CsX and PbX_2 powders (molar ratio = 2:1) was first placed into a furnace (Fig. 3)⁵¹ and then sintered at ~570–600 °C in an Ar gas atmosphere for 15 min. Consequently, different lengths of CsPbX_3 crystals were produced on the SiO_2/Si substrate.

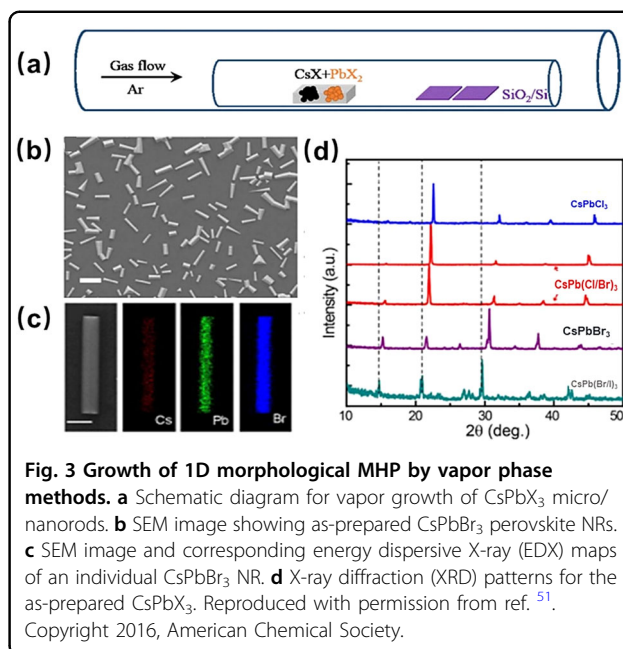


Fig. 3 Growth of 1D morphological MHP by vapor phase methods. **a** Schematic diagram for vapor growth of CsPbX_3 micro/nanorods. **b** SEM image showing as-prepared CsPbBr_3 perovskite NRs. **c** SEM image and corresponding energy dispersive X-ray (EDX) maps of an individual CsPbBr_3 NR. **d** X-ray diffraction (XRD) patterns for the as-prepared CsPbX_3 . Reproduced with permission from ref. ⁵¹. Copyright 2016, American Chemical Society.

Hot-injection methods

The hot-injection method is also commonly used for growing 1D halide perovskites. In 2015, Zhang and coworkers employed a hot injection approach to synthesize CsPbX_3 perovskite NRs by injecting the cesium precursor into a PbX_2 ($X = \text{Br}, \text{I}$) and octadecene (ODE) mixed solution with the assistance of oleic acid (OA) and oleylamine (OAm)⁵². They found that the OA was needed to decompose the precursor into monomers and coordinate the Pb^{2+} ions, and the OAm ensured a higher monomer concentration and weakened the reactivity of the Pb^{2+} precursor after nucleation, leading to controlled anisotropic growth. Liu and his coworkers changed the OA to OAm ratio, leading to the controlled growth of CsPbBr_3 crystals with various sizes and dimensionalities⁵³. With a gradual increase in the OAm proportion, 3D nanocubes were converted into 1D NRs and then into 2D nanoplatelets, suggesting that the OAm tuned the growth of the CsPbBr_3 . $\text{CsPb}(\text{Br}/\text{I})_3$ NRs with uniform rod-shape structures were also reported by combining PbBr_2 and PbI_2 ⁵⁴. More importantly, the morphology of the NRs (such as the lengths or diameters) were controlled by the reaction time.

Using an intermediate monomer reservoir synthetic strategy, Wang and colleagues achieved uniform, low-defect growth of CsPbBr_3 perovskite NRs. By substituting the Pb^{2+} in the CsPbBr_3 template with In^{3+} cations, intermediates such as CsPb_2Br_5 and $\text{Cs}_3\text{In}_2\text{Br}_9$ were also obtained⁵⁵. Moreover, some other studies produced lead-free 1D MHPs with low toxicity through hot injection⁵⁶. Among these, Chen et al. successfully

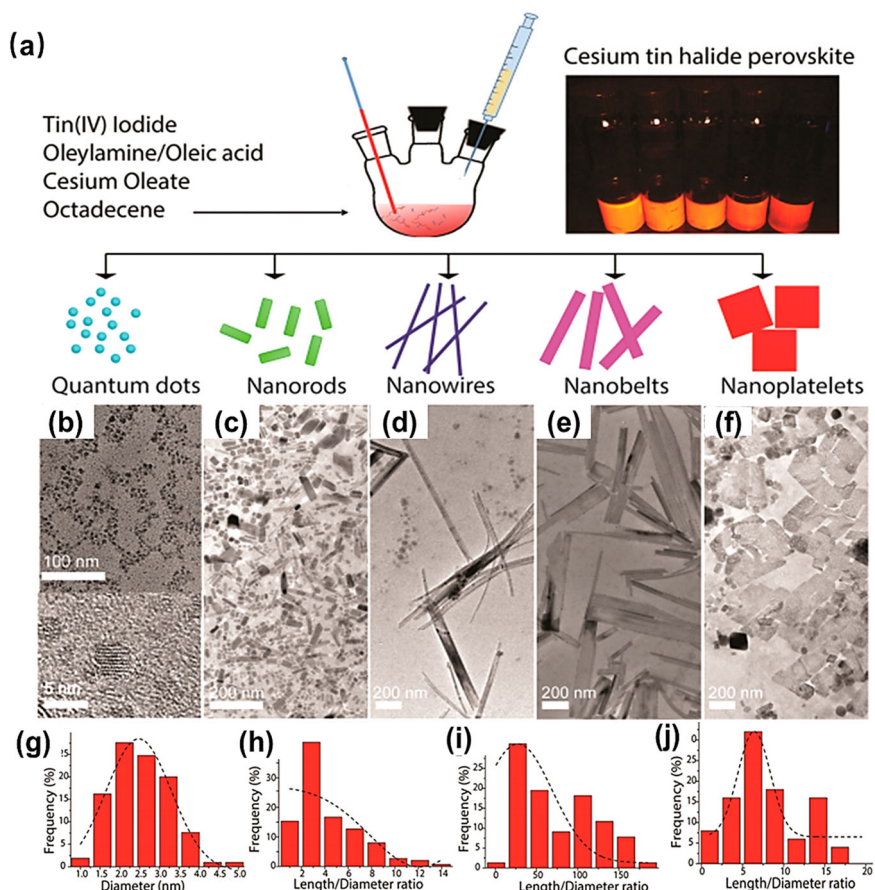
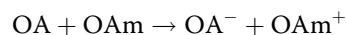


Fig. 4 Growth of 1D morphological MHP by hot-injection methods. **a** Scheme showing the synthesis of Cs_2SnI_6 and samples exposed to UV light. **b-f** TEM images of Cs_2SnI_6 . **g** Histogram showing the particle size distribution corresponding to Fig. 4b. **h-j** Histograms showing the diameter-length ratios for the samples in Fig. 4c–e. Reproduced with permission from ref. ⁵⁸. Copyright 2016, American Chemical Society.

synthesized a series of Sn-based inorganic MHP quantum rods using a solvothermal method⁵⁷, which displayed composition-dependent photoluminescence (PL) peaks ranging from 625 to 709 nm. Wang et al. prepared stable Cs_2SnI_6 NWs and NRs by reacting tetravalent tin (IV) iodide with cesium oleate at 220 °C by adding OA and OAm into the ODE⁵⁸. By varying the reaction time, they were able to control the morphology of the 1D Cs_2SnI_6 . Transmission electron microscope (TEM) images of samples taken at different times are demonstrated in Fig. 4⁵⁸, and these showed the evolution of the perovskite nanostructures. The OAm formed complexes with the Sn^{4+} ions, while the ODE suppressed the growth of Cs_2SnI_6 nanocrystals. OA and OAm displayed a synergistic effect in the controlled growth of 1D Cs_2SnI_6 ^{29,59}. The high electron-donating ability of deprotonated OA allowed it to interact strongly with specific crystal facets⁶⁰. OAm or other amines affected deprotonation of the OA, resulting in preferential and selective growth of Cs_2SnI_6 to form NWs and NRs via

the following reaction:²⁵



Template-assisted methods

The nucleation processes of perovskite NWs are difficult to control precisely with solution-phase methods, which often lead to random shapes coexisting rods, wires, plates, and cubes^{42,61}. To obtain well-defined structures, the template, such as anodized aluminum oxide (AAO), is introduced to guide the syntheses of oriented perovskite NWs. An ideal template should have a finely tunable pore diameter to control the product particle sizes and should be easy to integrate with other substrates for subsequent preparation of the NWs. The key factor in preparing high-quality perovskite NWs is selecting suitable templates with uniform template pores⁶². For example, Ashley and coworkers introduced an AAO template on a conductive fluorine-doped tin oxide (FTO) substrate to prepare NWs,

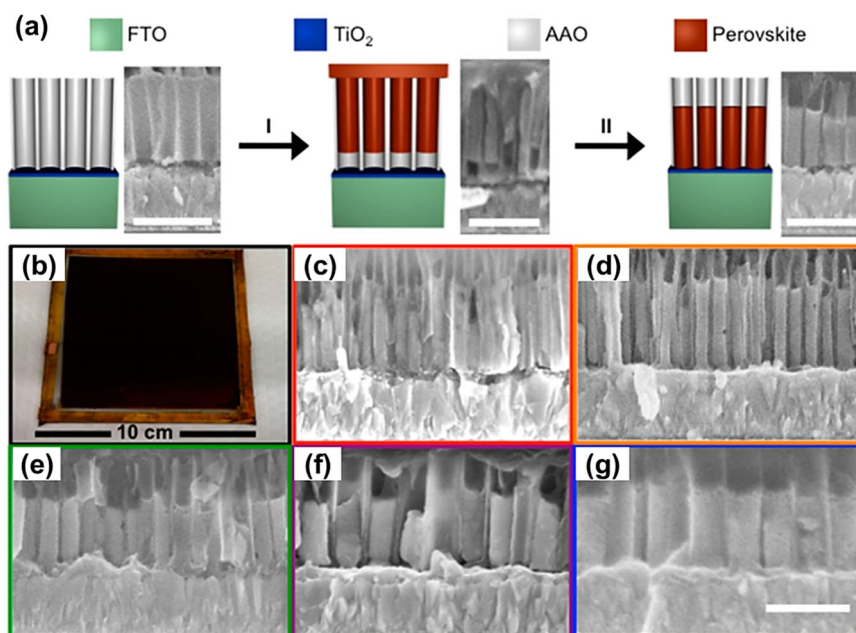


Fig. 5 Growth of 1D morphological MHP by template-assisted methods. **a** Scheme for the syntheses of 1D MHP NW arrays in AAO. Penetration of the precursor solution into the AAO pores (I). Dimethyl sulfoxide/chlorobenzene treatment (II). **b** Photograph of an NW array with a size of $\sim 9 \times 9$ cm. **c–g** SEM images with cross-sectional views of NWs with various diameters. Reproduced with permission from ref. ⁶³. Copyright 2016, American Chemical Society.

as shown in Fig. 5⁶³. In their work, aluminum was evaporated onto a TiO₂/FTO substrate, anodized to form an AAO template and then immersed in a MAPbI₃ precursor solution. However, an unavoidable drawback resulted because the AAO template could not be etched properly since MHPs are vulnerable to etchants²⁹.

To solve this problem, Oener et al. fabricated free-standing solution-based vertical NWs⁶⁴. They extruded the solution from the templates with a gradient pressure rather than embedding the perovskites into an AAO matrix. Notably, it was possible to peel off the prepared NWs and transfer them to different substrates for further experiments.

In addition, large-area MHP NWs, including those of MAPbI₃, MAPbBr₃, and all-inorganic Cs₂SnI₆, were produced. Using a vapor-solid-solid reaction process, Fan's team developed ordered MAPbI₃ NW arrays with thicknesses of 2 μm in porous alumina membranes (PAMs)⁶⁵. Pb nanoclusters were used as a reactant, and they were placed at the bottom of the PAM template to initiate growth of the MAPbI₃ NWs by reacting the nanoclusters with MAI vapor; this resulted in a precisely controlled geometry with an ultrahigh density up to $4 \times 10^9 \text{ cm}^{-2}$ for a large area of $\sim 9 \text{ cm}^2$. The porous alumina template (PAT) used previously to create 3D MASnI₃ NW arrays was used to synthesize MASnI₃ using this approach, which indicated the versatility of this template-assisted method⁶⁶. Similarly, MAI vapor was transported to the

PAT by argon gas, where it reacted with the Sn nanoclusters within the PAT nanopores. The MASnI₃ NWs displayed significantly improved stability compared with the polycrystalline MASnI₃ thin films due to effective blocking of the lateral paths enabling the diffusion of water or oxygen, leading to slower decomposition^{67,68}. Utilizing constructed templates to improve the stability of MHPs presents a novel and efficient approach to enabling practical applications.

Colloidal synthetic method

Since colloidal syntheses are commonly used to prepare perovskite nanocrystals (NCs), they were used to fabricate 1D MHP nanostructures exhibiting much narrower diameters than those prepared by other methods. Using an antisolvent recrystallization method, Zhu et al. prepared a mixed solution containing PbX₂, MAX, and the long-chain ammonium salt CH₃(CH₂)₇NH₃X (X = Cl/Br/I) in a high-polarity solvent (such as ACN) and then added a low-polarity solvent (such as toluene), thus generating accurately controlled perovskite NWs⁶⁹. Liu and coworkers synthesized CsPbBr₃ NWs from precursor powders through a colloidal process involving the assistance of organic ligands at room temperature⁷⁰. NWs with different lengths but highly uniform widths up to 32 nm were obtained by varying the reaction time, and they showed tunable optical emissions ranging from purple to green. The optical properties across the entire visible

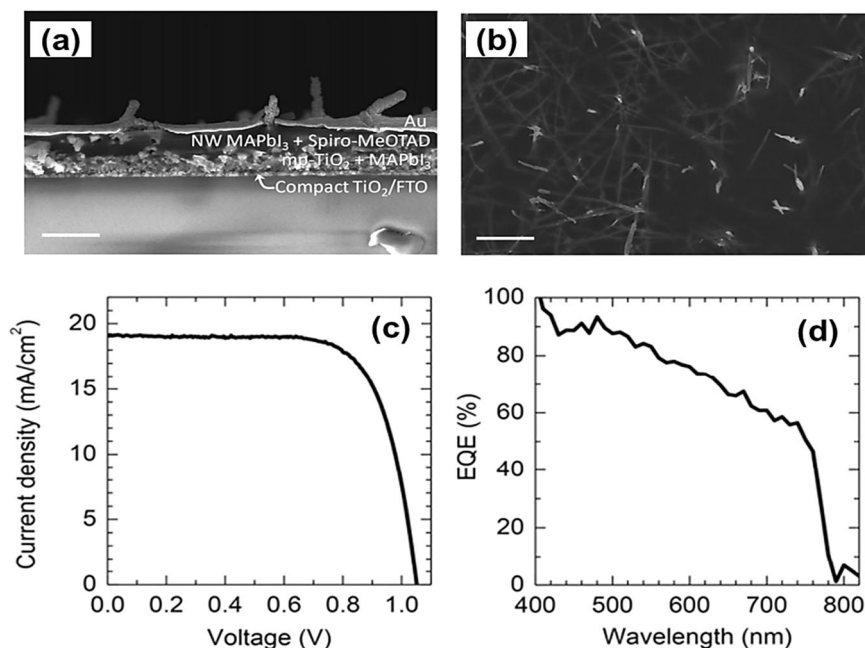


Fig. 6 Application of 1D morphological MHP NWs in solar cells. **a** Cross-sectional and **b** top-view SEM images of a solar cell device employing MAPbI₃ NWs. **c** Current-voltage curve and **d** EQE of the device based on MAPbI₃ NWs. Reproduced with permission from ref. ⁷⁴. Copyright 2015, American Chemical Society.

range were realized with an anion-exchange approach, which regulated the composition and controlled the morphology.

A more precisely controlled colloid synthetic method was developed recently, in which Imran et al. ⁷¹ introduced a short-chain aliphatic carboxylic acid to produce CsPbBr₃ NWs. The as-prepared NWs displayed PLQYs as high as 77%, and the color was tunable from green to blue. In another study, Chen's group presented a novel synthetic technique for fabricating ultrathin CsPbBr₃ NWs via a post-synthetic transformation starting from 0D Cs₄PbBr₆ perovskite NCs ⁷². The synthesized CsPbBr₃ NWs displayed blue PL with an emission quantum yield (QY) of 15.2%.

Applications of 1D morphological MHPs

Solar cells

Organic–inorganic MHP solar cells have demonstrated great potential for use in photovoltaic devices due to their unique properties, cost-effectiveness, high PCE, and solution processability. The PCEs of 3D perovskite solar cells (PSCs) have soared rapidly from 3.8% to 25.7%, and the latter level is comparable with those of commercial silicon solar cells ^{14,73}. The photovoltaic performance of a PSC mainly depends on the absorption of light, dissociation of excitons, and transport of charge carriers ²⁸. Compared with conventional 3D MHP nanocubes, NWs exhibit the advantages of longer carrier lifetimes and

higher external quantum efficiencies (EQEs), which make the NWs outstanding absorbers in solar cells ⁴¹. MAPbI₃ NWs were first introduced into perovskite solar cells by Park, Grätzel and coworkers ⁷⁴. They confirmed that the charge separation process was faster in 1D NWs than in 3D nanocubes due to better contact with the hole-transport materials. Moreover, the 1D NW films also displayed higher lateral conductivity than the 3D bulk film. The improved charge separation and conductivity led to better photovoltaic performance with an outstanding PCE of 14.71% under AM 1.5 G irradiation (Fig. 6) ⁷⁴. Therein, they used *N,N*-dimethylformamide to slightly dissolve the precoated PbI₂, which reacted with the MAI preferentially to construct the 1D NWs via a liquid-catalyst cluster mechanism. However, in this device design, the lack of reliable contacts between the perovskite material and the charge transport layers may retard the charge separation and transportation processes operating inside the whole device and lead to limited photovoltaic performance. A key challenge with such NW devices is to achieve intimate contact with the hole transport layer (HTL) and enable efficient hole extraction from the NWs. Chang et al. used an integrated approach ⁷⁵ and obtained a maximum PCE of 18.83% with MAPbI₃ NW solar cells exhibiting good stability. They employed a 4-(1,3-dimethyl-2,3-dihydro-1H-benzimidazol-2-yl)-*N,N*-diphenylaniline (N-DPBI)-doped poly{[*N,N'*-bis(2-octyldodecyl)-1,4,5,8-naphthalene diimide-2,6-diyl]-alt-5,5'-

(2,2'-bithiophene)} (P(NDI2OD-T2)) polymeric film as the electron transport layer (ETL) with encapsulation of atomic-layer-deposited (ALD) Al_2O_3 . Xiao et al. developed in situ growth of a 1D perovskite NW network triggered by using a Lewis basic amine over a 3D perovskite film to control the surface morphology, and this led to improved PCEs from 14.32% to 16.66% with negligible hysteresis⁷⁶. The amines passivated the trap states on the 3D perovskite surface and acted as rapid channels to boost charge transfer at the interface between the ETL and the 3D bulk perovskite film. The PSCs prepared with 1D NWs also maintained 96% of their initial PCEs after storage in ambient air for 30 days without encapsulation. Liao et al. incorporated all-inorganic CsPbX_3 NWs prepared by a solution-dipping approach and regulated the compositions of the NWs via a halide exchange method⁷⁷. The CsPbI_3 and CsPbBr_3 NW-based PSCs exhibited low PCEs of 0.11% and 1.21%, respectively, which might be attributed to the partial coverage of the CsPbX_3 NWs leading to severe recombination and reduced light harvesting. Despite the poor photovoltaic performance, this device exhibited significantly improved thermal and humidity stability over the organic counterparts.

Chen et al. synthesized a series of high-quality CsSnX_3 ($X = \text{Cl}/\text{Br}/\text{I}$) NRs by using a solvothermal method for the first time⁵⁷. These quantum rods displayed wide PL emission bands ranging from 625 nm to 709 nm, indicating tunable optical properties. They achieved PCEs as high as 12.96% for CsSnI_3 (9.66% for CsSnCl_3 , 10.46% for CsSnBr_3), revealing the potential of Sn-based NRs in photovoltaic devices.

In principle, perovskite NW-based solar cells have great potential and a promising future. However, their PCEs are still lower than those of their 3D counterparts for the following two main reasons: first, the poor contacts between the perovskite NWs/ETLs and perovskite NWs/HTLs result in reduced charge transport; furthermore, it is challenging to prepare template-free and vertically oriented NWs^{29,74}. If a template is involved, light absorption and charge transport by the MHP will be negatively affected. Considering that charge transport must occur along the axes of the NWs, the performance of the device can be improved only when the NWs adopt well-aligned perpendicular orientations between the two electrodes. A future research theme for the development of NW-based solar cells could involve the preparation of vertical and template-free NWs and the improvement of their contacts with the neighboring transport layers.

Lasers

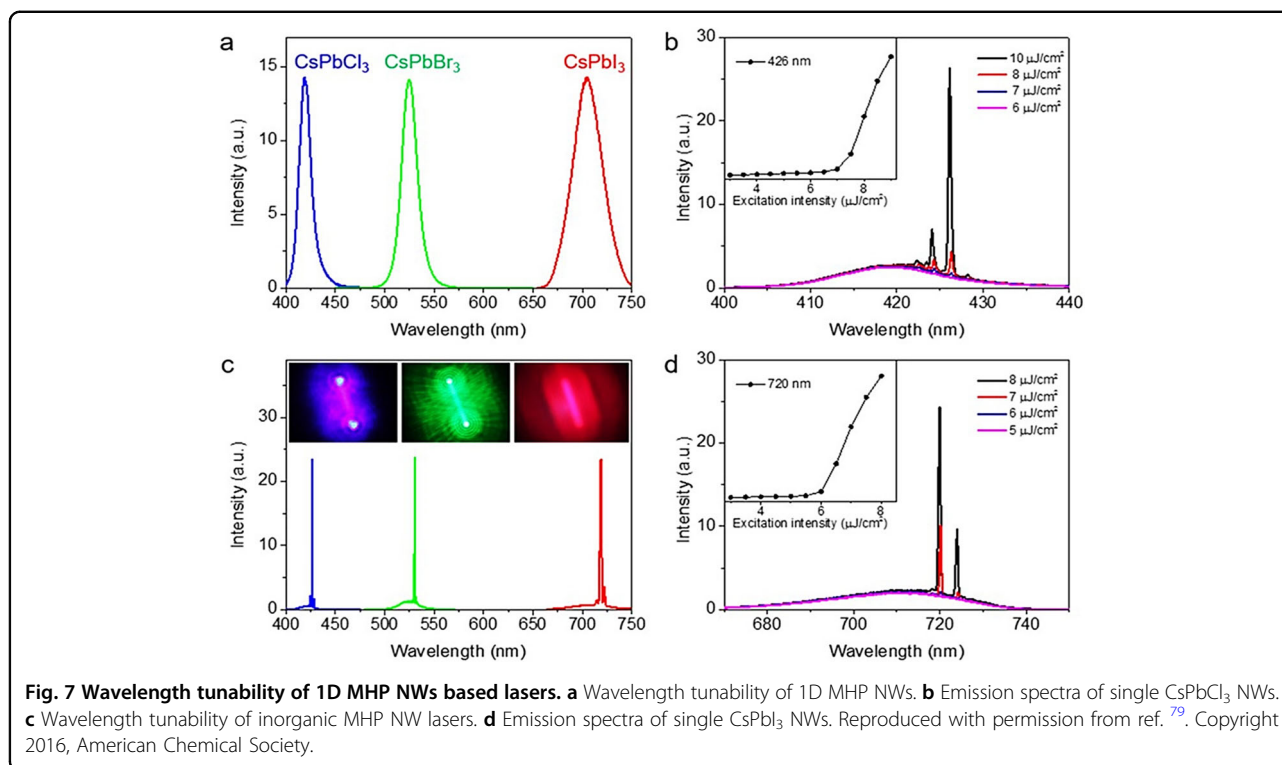
Compared to 0D nanocrystals, 2D nanosheets, and 3D nanocubes, 1D MHP NWs have been considered more promising candidates for utilization in lasers owing to their excellent properties; they are efficient waveguides

with highly localized coherent outputs, compact physical sizes and strong anisotropies⁷⁸. They serve as waveguides along the axial direction and form Fabry–Perot cavity at the two end facets to enable optical amplification. Zhu et al. demonstrated the first MHP NW-based laser, which operated at room temperature and was based on solution-prepared MAPbI_3 NWs with subwavelength dimensions and smooth facets⁴². They transferred a few well-dispersed NWs to a Si/SiO_2 substrate via a dry contact method, and a 402 nm pulsed beam was applied as the pump source. After reaching the lasing threshold, the NWs exhibited a sharp emission peak centered at 787 nm, showing broad and tunable lasing with a low threshold of 220 nJ cm^{-2} and an extremely high quality factor ($Q \sim 3600$). Because they exhibited limited nonradiative recombination and little charge-carrier trapping, the QYs approached 100% for these NWs. In another study, Park et al. used a chemical vapor transport approach to prepare CsPbX_3 MHP NWs with homogeneous compositions, ordered growth directions, and good crystallinities⁷⁹. These NWs showed lasing behavior at low thresholds ($3 \mu\text{J}/\text{cm}^2$) and achieved high quality factors exceeding 1200 in ambient environments (Fig. 7)⁷⁹. By regulating the compositions of these NWs, the emission colors were tunable from deep blue to green and red. Although the MAPbX_3 NWs displayed excellent lasing performance, they may degrade when exposed to continuous illumination, heat and a high current load⁸⁰.

In contrast, single-crystalline NWs comprising FAPbX_3 and CsPbX_3 showed similar performance but improved temperature and moisture stability^{81,82}. Pan's group prepared CsPbX_3 alloy perovskite micro/nanorods using vapor-phase deposition. These single-crystalline high-quality 1D CsPbX_3 analogs with triangular cross-sections displayed PL that was tunable from 415 nm to 673 nm by controlling their compositions⁵¹. They also acted as effective Fabry–Perot cavities with low lasing thresholds and high quality factors of $\sim 14.1 \mu\text{J cm}^{-2}$ and 3500, respectively. The lasing QY of these NWs was $\sim 100\%$ due to the negligible charge carrier trapping. Similarly, Jin's group grew single crystals of CsPbBr_3 , CsPbCl_3 and $\text{CsPb}(\text{Br},\text{Cl})_3$ with well-defined rectangular facets, and these demonstrated stable CsPbX_3 emission with negligible degradation after 8 h⁴⁵. Interestingly, the CsPbBr_3 NWs maintained their surface morphology for over 6 months under ambient conditions. All of these results indicated that these inorganic NWs are promising alternatives for optoelectronic applications.

Photodetectors

Photodetectors (PDs), which harvest optical signals and convert them into electric signals, are used in many applications, including image sensing, sensing for the Internet of Things (IoT), optical communications, and



environmental monitoring^{66,83}. When the PDs are exposed to photoirradiation, electron-hole pairs are generated inside the devices, and the separated electrons and holes drift under the applied external bias. Ultimately, the photocurrent is measured by collecting the electrons at the anode⁸⁴. In comparison to 3D bulk MHPs, the 1D NW semiconductors have well-defined nanostructures with larger surface-to-volume ratios, higher crystallinities, lower trap densities, reduced recombination, and longer lifetimes for the photogenerated carriers. They offer more confined and efficient pathways for rapid transport of the photoinduced charge carriers inside the 1D channels⁸⁵. Horváth et al. first developed 1D NW-based PDs, in which the NWs produced by slip-coating exhibited mean diameters of up to 400 nm and showed a responsivity (R) of 5 mA/W⁴¹. 1D MHP PDs are rarely reported because it is difficult to control the random distributions of the 1D NWs, which inhibits the collection of the photocarriers. Therefore, it is crucial to prepare NWs with controlled morphologies and enhanced performance. By regulating the crystallization process, Deng et al. developed transparent and uniform MAPbI₃ NWs as PD arrays based on polyethylene terephthalate (Fig. 8)⁸⁶. Well-defined NW networks were developed by controlling the crystallization process. The constructed PDs showed a narrower photocurrent range than PDs based on randomly oriented NWs, with a switching ratio of 300, a normalized detectivity of 1.02×10^{12} Jones, and an equivalent dark current-

derived shot noise of 4.73×10^{-15} A Hz^{-1/2}. Furthermore, this device demonstrated excellent flexibility during bending 10,000 times.

Similarly, horizontal CsPbX₃ (X = Cl, Br, I) NW networks with well-controlled orientations along the (001) plane were prepared by the vapor-phase method^{50,87}. Han et al. developed lead-free CsSnX₃ NW arrays deposited on mica in a three-zone CVD furnace via solid-source chemical vapor deposition (SCVD)⁸⁸. By controlling the type, mass, temperature and growth time, CsSnX₃ NWs with various compositions and grain sizes were obtained. The as-prepared CsSnBr_{3-x}I_x (x = 0, 2, 3) NW arrays showed very strong PL with bandgaps varying from 1.34 to 1.84 eV. Moreover, the as-prepared CsSnI₃ NW arrays were utilized for the first time as the channel materials for near-infrared photodetectors, and they exhibited superb photodetection performance with rise and decay time constants of 83.8 ms and 243.4 ms, respectively. The aligned NW arrays resulted in improved photodetection⁸⁸. Using a blade-coating method, Jie's group developed an aligned MAPbI₃ NW array, which was suitable for processing microwire arrays with large areas on flexible substrates⁸⁹.

Benefitting from the anisotropic responses to polarized light signals, 1D MHPs with anisotropic morphology can act as polarization-sensitive optical switches, integrated photonic circuits, high-resolution detection, and near-field imaging^{90,91}. Anisotropic optical absorption by

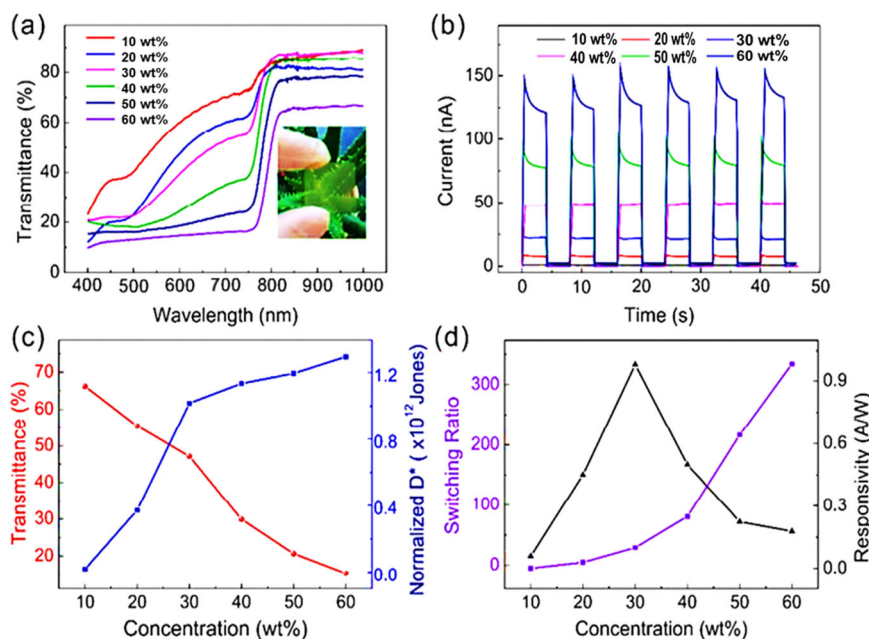


Fig. 8 Effect of the precursor concentration on MAPbI₃ NW-based PDs. **a** Transmittance of organolead triiodide perovskite networks as a function of the precursor concentration. **b** *I*-*t* curves for networked PD arrays. **c** Transmittance and normalized detectivity as a function of the precursor concentration. **d** Effect of precursor concentration on the responsivity and switching ratio. Reproduced with permission from ref. ⁸⁶. Copyright 2015, American Chemical Society.

MAPbI₃ PDs was first demonstrated by Gao et al., which underscored the advantages of using these NW arrays in polarized PDs⁹². OA-passivated PDs exhibited superior detectivity of 2×10^{13} Jones, which were higher than those of commercialized Si-based photodetectors (4×10^{12} Jones). Moreover, the maximum photocurrent was obtained when the polarization direction was parallel to the NW orientation axis, while the minimum photocurrent was obtained with perpendicular polarization. Similarly, a sensitive PD based on a 1D CsPbBr₃ single-crystal NW array was assembled by Feng and coworkers, who used a micropillar-structured template-assisted method⁹³. A high $I_{\text{on}}/I_{\text{off}}$ ratio of 103, an excellent responsivity over 1000 A W^{-1} , and a fast response speed ($21.5 \mu\text{s}$ for the rise and $23.4 \mu\text{s}$ for the decay) were achieved. They also found that the high aspect ratios of 1D NWs induced good anisotropic absorption, which contributed significantly to the polarized light sensitivity of the 1D NWs.

High-performance PDs were also developed by using a single 1D perovskite NW^{86,94}. Shoaib et al. grew ultralong CsPbBr₃ NWs via controlled vapor phase growth, and they showed well-defined cross sections and smooth surfaces⁹⁵. The resulting CsPbBr₃ NW-based PDs exhibited a high responsivity and a fast response speed of 4400 A W^{-1} and $252 \mu\text{s}$, respectively.

In addition, nontoxic NW PDs have also been prepared with MASnI₃ NW arrays⁶⁶. The PDs showed quick

responses to light with rise and decay times of 1500 ms and 400 ms, respectively. Compared to a planar device, the decay of the light current was approximately 500 times slower for the NW-based device.

Light-emitting diodes

Due to their superb optoelectronic properties, including low exciton binding energies and long carrier diffusion lengths (up to the micrometer level), 3D perovskites display outstanding photovoltaic performance. However, these materials provide reduced light-emitting efficiencies with low injected carrier densities (less than 10^{15} cm^{-3}), which limits the performance of the perovskite LEDs⁹⁶. For the charge carriers, there is a competition between the radiative recombination and nonradiative trapping processes. When the former dominates the dynamic process, high-performance LEDs can be realized. 1D MHP NWs with high crystallinity and superior optical properties have been used to assemble LEDs. Wong et al. fabricated a hybrid perovskite (MAPbBr₃) NR array and then converted it to MAPbI₃ via an anion exchange technique used at low temperatures while preserving the morphology⁴⁴. The MAPbBr₃ NR-based LED showed a green electroluminescence (EL) peak at 533 nm with a full width at half maximum (FWHM) of 26 nm, while the converted MAPbI₃ arrays showed infrared EL at 782 nm with a FWHM of 41 nm. In the work of Guo et al., 1D CsCdBr₃ NRs were prepared via a facile thermal-injection

method⁹⁷. However, the low PLQY hindered their use in LEDs. PbBr_2 was selected as the dopant for CsCdBr_3 NRs to improve their EL properties. When $\text{PbBr}_2:\text{CdBr}_2 = 1:4$ (molar ratio), the perovskite NRs showed a PLQY of 48% and a pure-blue emission centered at 459 nm. In addition, they were employed as the active layer in a LED and exhibited a maximum brightness of 225 cd m^{-2} and an EQE of 0.35%. Bi and his coworkers prepared CsPbI_3 NW clusters in a nonpolar solvent system by using a ligand-assisted reprecipitation approach⁹⁸. These NW clusters displayed an emission peak centered at 600 nm and a large PLQY of 91% with excellent environmental and structural stability. An excellent EQE of 6.2% and a maximum EL luminance of 13644 cd m^{-2} were obtained for the corresponding LED device. Although many studies have been published on NW-based LEDs, there are still shortcomings and challenges restricting their development relative to those of other low-dimensional MHPs, particularly 0D nanocrystals. Issues including lower PLQYs, worse color purity and poor tunability of the optical properties need to be overcome.

Other applications

If high-density PDs (at the level of millions per cm^2) are assembled, an image sensor can be fabricated, and every single PD could be a pixel for the image. Image sensors have attracted considerable interest for use in many advanced fields, such as the medical, artificial intelligence, and wearable electronics fields. Deng et al. prepared large-area and horizontally aligned MAPbI_3 microwire PDs based on the conventional configurations of field-effect transistors⁸⁹. They also assembled an image sensor comprising 21×21 pixels, which demonstrated letters under different bending conditions. To integrate more single PD devices with optimal performance, vertical alignments of the NWs have been explored. Gu and coworkers assembled image sensors based on 3D MHP NW photodiodes with ultrahigh NW density of $\sim 4 \times 10^8\text{--}10^9 \text{ cm}^{-2}$. These integrated devices recognized optical patterns, such as “C”, “H”, “K”, and even a symbol for the heart⁶⁵. Although there were only 1024 pixels displayed therein, the results implied that the NW arrays have great potential for use as high-resolution image sensors because the size of each NW pixel can be hundreds of nanometers, leading to a dramatic increase in the number of pixels. The NWs were well protected by the template, which retarded the diffusion of oxygen molecules and moisture, and this improved the stability. Despite the satisfactory device performance, 1D nanostructured MHPs still suffer from high surface trap states and undesirable dangling bonds, which compromise the performance in photodetection and the long-term stability and seriously impede their application^{29,99}.

1D nanostructured MHPs have also been employed as high-performance FETs due to their low defects and high charge carriers. Chen and coworkers prepared FETs based on a bilayer structure comprising an organic semiconductor and CsPbI_3 NRs, in which the organic semiconductor served as the pathway for the injected photoinduced carriers and the CsPbI_3 NRs served as light absorbers¹⁰⁰. The FET showed p-type characteristics with a cutoff V_G of $\sim -40 \text{ V}$ and a constant V_D of -30 V . Finally, these FETs demonstrated efficient and stable performance with high γ up to 4300 A W^{-1} and a photo-dark current ratio of 2.2×10^6 . By introducing different organic semiconductors such as PDVT-10 and N2200, Chen et al. developed FETs exhibiting p-type and n-type behaviors, respectively, and displaying strong light and gate modulation¹⁰¹.

In another important application, memory devices using 1D MHPs as the switching layers have been reported because of their intrinsic hysteresis and massive channels for charge transfer. Zhao's group developed light-induced resistive switching (RS) based on individual MAPbI_3 micro/nanofibers¹⁰². The RS effect was ascribed to the redox reactions occurring at the interface between the MAPbI_3 and the Ag electrode, and the MAPbI_3 can be regarded as the solid electrolyte. In another study, Poddar et al. applied a vapor-phase approach to prepare ordered monocrystalline MAPbI_3 quantum wire/NW arrays in the nanochannels of a porous alumina membrane, thereby forming a Ag/MAPbI_3 quantum wire/NW/Au structure¹⁰³. This device displayed a superior performance with an ultrafast switching speed of $\sim 100 \text{ ps}$, a record endurance of $\sim 6 \times 10^6$ cycles, and a long duration of over 2 years. Moreover, the team downscaled the device to a lateral dimension of 14 nm and an area of 76.5 nm^2 for single bit storage.

Molecular-level one-dimensional perovskites

Syntheses of 1D molecular MHPs

In molecular 1D MHPs, the metal halide octahedra ($[\text{BX}_6]^{4-}$) participate in corner sharing, face sharing and edge sharing to build 1D networked chains with the surrounding organic cations^{104,105}. There are various types of chains, including linear, bilinear, zigzag, and tubular, and their chemical formulas depend on the connecting methods and the organic cations. Unlike morphological 1D MHPs, molecular 1D MHPs are large crystals comprising assemblies of $[\text{BX}_6]^{4-}$ quantum wires (QWs)^{13,106,107}. In 1995, the first 1D MHPs were reported by Mitzi and coworkers, and they had the formula $[\text{NH}_2\text{C}(\text{I})=\text{NH}_2]_2(\text{CH}_3\text{NH}_3)_m\text{Sn}_m\text{I}_{3m+2}$ ($m = 1$)^{108,109}. As perovskite-related materials, molecular 1D MHPs have attracted tremendous research interest during the last several years. Mao and coworkers found that 1D $(2,6\text{-dmpz})_3\text{Pb}_2\text{Br}_{10}$ contained a single corner-sharing chain of

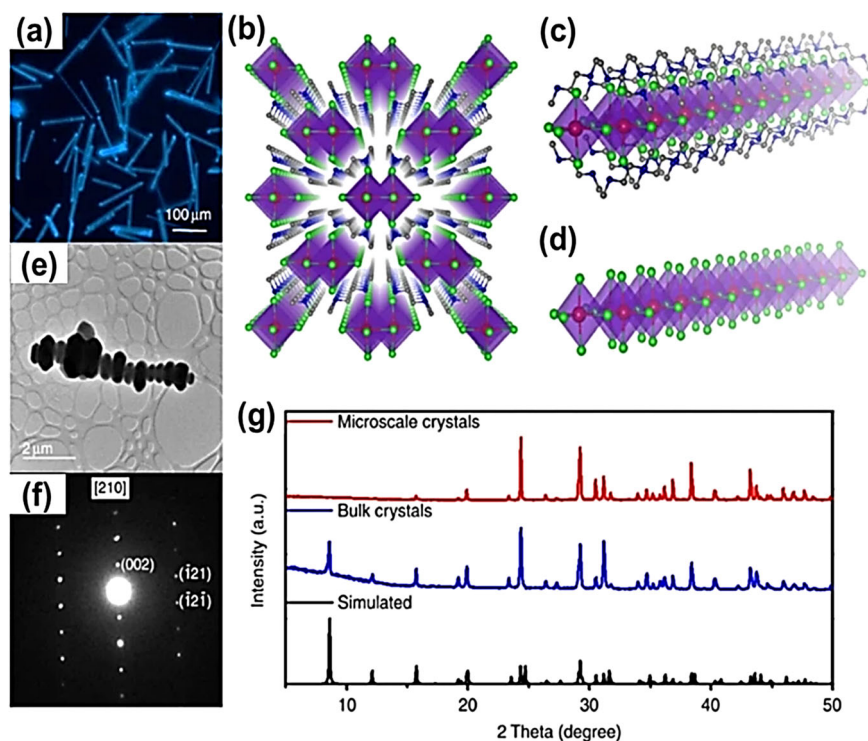


Fig. 9 Characterization of 1D molecular $C_4N_2H_{14}PbBr_4$. **a** Optical image showing 1D MHP single crystals. **b** Structure of 1D $C_4N_2H_{14}PbBr_4$. View of an individual lead bromide quantum wire with **c** and without **d** wrapped organic cations. **e** TEM image of microscale 1D perovskite crystals. **f** Electron diffraction pattern along the [210] zone axis. **g** Powder XRD patterns for bulk and microscale 1D MHP crystals, as well as simulated patterns. Reproduced with permission from ref. ¹¹¹. Copyright 2017, Nature Publishing Group.

lead bromide and a mixture of corner- and edge-sharing dual chains¹¹⁰.

The recent interest in molecular 1D MHPs was greatly stimulated by the development of $C_4N_2H_{14}PbBr_4$ by Yuan et al., in which core-shell QWs were constructed with edge-sharing $[PbBr_4]^{2-}$ and surrounded by $C_4N_2H_{14}^{2+}$ organic cations (Fig. 9)¹¹¹. Because of the formation of self-trapped excitons (STEs) and the presence of strong quantum confinement, these unique 1D MHPs displayed intriguing bluish white broadband emission under UV irradiation. PLQYs of 18–20% and 10–12% were obtained for single crystals and microscale crystals, respectively. Interestingly, Yuan et al. also generated significant improvement and a pressure-induced PL of ~90% at 2.8 GPa with the 1D hybrid metal halide $C_4N_2H_{14}PbBr_4$ ¹¹².

Mn ions have been introduced in a facile one-pot synthetic method to dope these 1D MHPs and improve the efficiency of white emission¹¹³. Taking advantage of the Mn dopant emission and the STE emission of the 1D MHP itself, tunable and broad bright white emission was achieved with color rendering indexes (CRIs) of up to 87 and improved PLQYs of up to 28%^{113,114}. Researchers also prepared 1D $C_4N_2H_{14}PbCl_4$ by replacing the Br atoms with Cl atoms within the edge-sharing octahedral $PbCl_2$ chains $[PbCl_4^{2-}]_{\infty}$ separated by the organic $C_4N_2H_{14}^{2+}$

cations¹¹⁵. Calculations based on density functional theory (DFT) indicated that two emission bands were attributed to the STEs and vacancy-bound excitons of these 1D MHPs.

Li and coworkers also reported 1D dual-emissive MHPs, $(C_{12}H_{18}N_6)Pb_2Cl_{10} \cdot H_2O$, displaying tunable white light emission from “cold” to “warm” by changing the excitation wavelength¹¹⁶. The combined results of the emission spectra and the DFT study revealed that the broadband emissions of these MHPs aided the formation of the STEs. In another study, toxic Pb^{2+} ions were substituted by Sn^{2+} to form lead-free 1D $C_4N_2H_{14}SnBr_4$. With continuous UV irradiation, this nonemissive and kinetically stable 1D $C_4N_2H_{14}SnBr_4$ underwent a structural transformation to form the thermodynamically stable 0D Sn bromide hybrid, which was also confirmed computationally¹¹⁷.

To address the toxicity of Pb, researchers have studied 1D MHPs containing other nontoxic metals, such as Sb, Bi, and Sn, with electronic structures similar to those of the Pb-containing counterparts^{118–121}. Mousdis et al. synthesized zigzag-chain 1D Sb-based MHPs $[CH_3SC(NH_2)_2]_2SbX_5$ containing corner-sharing $[SbX_6]$ octahedra that were separated by $CH_3SC(NH_2)_2^{2+}$ cations¹¹⁸. Although they exhibited large E_g values and low performance, these lead-free materials are nontoxic and stable and could be

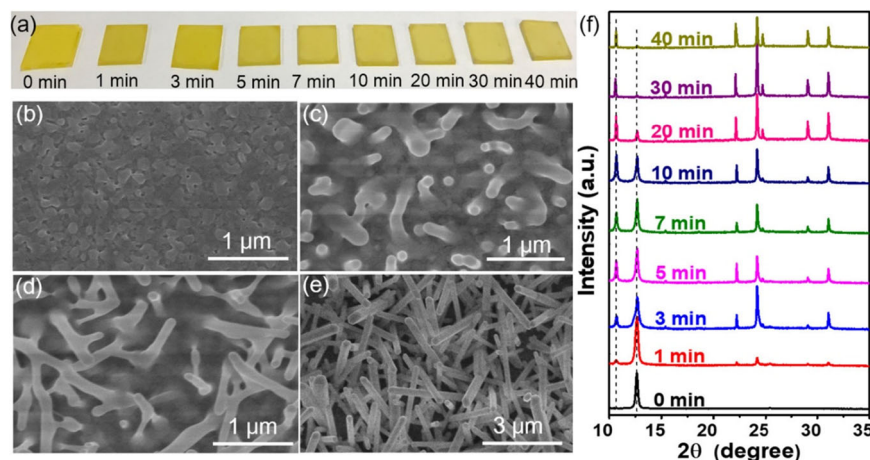


Fig. 10 Example of 1D sulfur-based $(\text{CH}_3)_3\text{SPbI}_3$ NRs. **a** Optical images of PbI_2 films after dipping in a $(\text{CH}_3)_3\text{SI}$ solution for different periods of time. Top-view SEM images of a PbI_2 film dipped in a $(\text{CH}_3)_3\text{SI}$ solution for **b** 0 min, **c** 5 min, **d** 10 min, and **e** 30 min. **f** XRD patterns for the treated PbI_2 films. Reproduced with permission from ref. ¹²⁴. Copyright 2020, Elsevier B.V. and Science Press.

potential alternatives for use in optoelectronic applications. In addition, Zhang et al. developed lead-free $(\text{C}_6\text{H}_{14}\text{N})_2\text{SbCl}_5$, which consisted of hexamethylenimine and a 1D $[\text{SbCl}_5]_n^{2-}$ polyanionic zigzag chain, and this showed nonlinear optical properties that were switchable above room temperature¹¹⁹. They found that a structural phase transition occurred in the presence of the order-disorder conformation of the organic cation. The difference in molecular conformations made the material promising for exploring novel switching devices. Dammak and coworkers prepared the organic-inorganic MHP $(\text{C}_6\text{H}_{14}\text{N})_2\text{BiBr}_5$ by the slow-evaporation method¹²⁰. The strongly bound excitons caused radiative recombination of the 1D QWs and strong blue emission. In another study, Zhang et al. prepared the 1D lead-free metal halide $(\text{C}_6\text{H}_{14}\text{N})_2\text{BiI}_5$ by slow evaporation of a precursor solution containing 4-methylpiperidinium and bismuth trioxide dissolved in concentrated hydroiodic acid¹²¹. This light-absorbing hybrid material with zigzag chains was photoconductive, moisture stable and environmentally friendly, and it exhibited a narrow and direct E_g of ~ 2.02 eV and a long lifetime, indicating that it is a promising candidate for optoelectronic applications. Hu et al. reported a series of 1D MHPs based on $[4\text{ApyH}]\text{Sb}_x\text{Bi}_{1-x}\text{I}_y\text{Br}_{4-y}$, wherein 4-ApyH stands for the 4-aminopyridine cation¹²². They systematically studied the structures and properties of these materials by investigating the effects of the halogen ions (Br^- and I^-) and the metal ions (Sb^{3+} and Bi^{3+}) and found that the compositions played significant roles in determining the optical bandgaps, which ranged from 1.94 eV ($[4\text{ApyH}]\text{BiI}_4$) to 2.73 eV ($[4\text{ApyH}]\text{SbBr}_4$). Moreover, the conductivity of $[4\text{ApyH}]\text{Sb}_x\text{Bi}_{1-x}\text{I}_4$ was increased significantly from $\sim 1.00 \times 10^{-15}$ to 2.14×10^{-8} S cm^{-1} with an increase in the Sb ratio.

In addition to metal halide QWs, 1D MHPs containing tubular metal halides were discovered by Lin and his coworkers¹²³. The 1D hexamethylenetetramine (HMTA, $\text{C}_6\text{H}_{13}\text{N}_4^+$) lead bromide nanotubes, $(\text{C}_6\text{H}_{13}\text{N}_4)_3\text{Pb}_2\text{Br}_7$, were synthesized by a slow solution-diffusion approach¹²³. The 1D tubular structure was completely isolated and localized, and it showed the intrinsic properties of a single tube. Because of the STEs, the 1D structures showed a large Stokes shift with broad yellowish-white emission and a PLQY of $\sim 7\%$. The 1D tubular structures displayed relatively lower PLQYs than the 1D NW structures, which may be attributed to the presence of more nonradiative pathways in the 1D tubular structures. However, the amine N-H bonds were easily hydrolyzed with moisture, leading to the loss of perovskite stability. It is highly desirable to explore novel and stable nonamine perovskite materials. In the work of Hu et al., 1D sulfur-based perovskite-like $(\text{CH}_3)_3\text{SPbI}_3$ NR arrays were fabricated via a two-step solution phase synthetic method (Fig. 10)¹²⁴. Due to the strong binding forces of the cationic $(\text{CH}_3)_3\text{S}^+$ and the $[\text{PbI}_6]^{4-}$ octahedra, the morphology and crystal structure remained unchanged for 60 days under ambient conditions. Similarly, Rahman et al. prepared moisture-stable trimethylsulfoxonium lead triiodide $(\text{CH}_3)_3\text{SOPbI}_3$ 1D NR arrays in aqueous media, which exhibited no change in the hexagonal crystal structure over 50 days¹²⁵. The superb moisture stability of $(\text{CH}_3)_3\text{SOPbI}_3$ originated from strong electrostatic interactions between the TMSO^+ and $[\text{PbI}_6]^{4-}$ polyhedra.

Applications of 1D molecular MHPs

The current research interest in 1D molecular MHPs is focused on fundamental studies of the structure-property relationships, including synthetic methods and

characterizations of the photophysical and electronic properties¹⁰⁴. Potential uses of the 1D molecular MHPs constitute a relatively new research topic that has not yet been well explored. Generally, 1D molecular MHPs with large bandgap energies (E_g) and exciton binding energies (E_b) may be suitable for use in lighting systems such as LEDs and phosphors based on the recombination of electrons and holes. In contrast, 3D MHPs with smaller E_b values are suitable for photovoltaic applications based on the transport of charge carriers, such as in solar cells and PDs^{12,104,126}. Therefore, combinations of 1D and 3D MHPs may provide exciting opportunities enabling a wide range of applications.

Solar cells

1D perovskites exhibit superb stability because of the skeletal strength attributable to the “shoulder to shoulder” arrangement of $[\text{PbX}_6]^{4-}$ and the protection from organic cations^{11,30,127,128}. Although the high E_b values of 1D MHPs retard charge transport, combinations of 1D and 3D MHPs provide extraordinary opportunities for advancing photovoltaics. By directly incorporating large organic cations into the 3D perovskite or postprocessing large cations on top of the 3D perovskite film, multi-dimensional films can be produced that are environmentally stable and feature excellent photovoltaic properties. In a representative study, 1,1,1-trifluoroethylammonium iodide (FEAI) was employed by Bi and coworkers to enhance the efficiency and long-term stability of a device¹²⁹. To maintain a constant exciton binding energy and bandgap, they added less than 10 molar% FEAI to the precursor solution of MAPbI_3 . They obtained a better surface morphology for the perovskite film with improved coverage, increased crystallinity, and reduced roughness. The solar cells reached a maximum PCE of 18% with 3% addition of FEAI. The stability to moisture was improved by the presence of the CF_3 terminal group, which was hydrophobic and retarded degradation of the MHP. Fan et al. incorporated 2-(1H-pyrazol-1-yl)pyridine (PZPY) into 3D MHPs, leading to the formation of a series of 1D or 1D/3D heterojunctions, realizing a thermodynamic self-healing ability with improved long-term stability¹³⁰. The 1D/3D MHPs displayed greater thermodynamic stability than pure 3D MHPs. The PCE of the 1D/3D device was reversible during temperature cycling (25–85 °C), whereas a reference device failed completely after five cycles. Liu et al. proposed a lattice-matching structure prepared by adding the 1D PbI_2 -bipyridine (BPy) into 3D MHPs, and this led to enhanced stability of both the film and the device¹³¹. In the work of Yu et al., hydrazinium (HA) was employed to stabilize α -phase FAPbI_3 by forming a 1D/3D hybrid perovskite structure¹³². Gao et al. applied thiazole ammonium iodide (TAI) to generate a 1D passivation

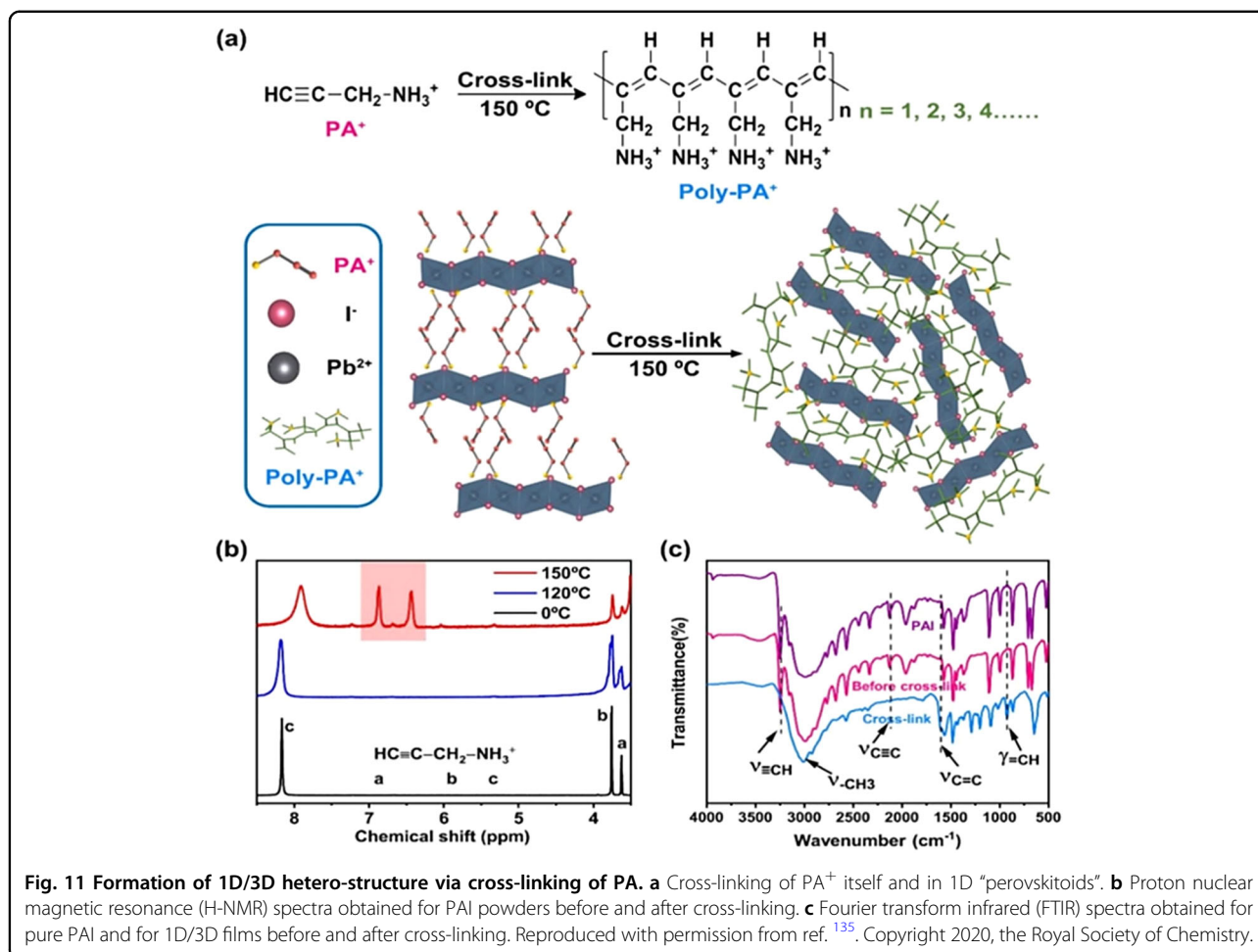
layer of TAPbI_3 on top of a 3D MHP, which passivated defects, enhanced charge transfer, blocked ion migration, and resulted in a higher PCE of 18.97% and better long-term operational stability over 2 months under ambient conditions¹³³. Similarly, Xu et al. employed a 1D PyPbI_3 (Py = pyrrolidine) perovskite to stabilize the black perovskite phase and enhance the performance of the resulting device¹³⁴. In another study, a thin layer of in situ cross-linked propargylammonium (PA^+) was used by Chen’s group to generate a 1D/3D heterostructure; this facilitated interfacial charge transport and released the residual tensile strain of 3D MHPs (as shown in Fig. 11)¹³⁵. Very recently, Kong et al. developed a novel perovskite using 2-diethylaminoethylchloride hydrochloride (DEAECCL), which facilitated crystallization and provided better crystallinity, leading to improved charge transport and reduced remnant tensile strain in the 3D perovskite film¹³⁶. A maximum PCE of up to 22.9% was realized along with excellent device stability.

Light-emitting diodes

Single-luminescent materials have been identified as promising candidates for preparing next-generation white LEDs. However, there is an inevitable optical loss because the current white light source is a yellow phosphor-coated blue LED¹⁰⁴. To address this issue, Lin et al. developed single-component-based white lighting with an environmentally friendly 1D CsCu_2I_3 perovskite¹³⁷. It displayed a broad PL emission peak at 568 nm and a FWHM of ~75 nm for the white light resulting from black body radiation. Moreover, it showed excellent photostability and retained 95% of the initial PL intensity after continuous laser excitation for 750 min. Mo et al. produced 1D lead-free CsCu_2I_3 single crystals via inverse temperature crystallization, and it showed yellow emission and good air stability¹³⁸. A quasi core-shell structure was formed in which the $[\text{Cu}_2\text{I}_3]^-$ chains were spatially separated by the Cs^+ ions in the 1D CsCu_2I_3 lattice. A record PLQY of 50.4% was achieved in the presence of OA. Furthermore, when combining the CsCu_2I_3 yellow phosphor with blue LEDs for white light applications, it provided continuous operation for over 580 h in air. For EL applications, a highly stable yellow LED based on CsCu_2I_3 was proposed by Ma et al.¹³⁹. They prepared tightly packed CsCu_2I_3 by antisolvent crystallization, and it exhibited a PLQY of 20.6%. The yellow EL resulted in broadband emission at 550 nm with a maximum luminance of 47.5 cd m^{-2} and an excellent EQE of 0.17%, which was ascribed to STE emission (Fig. 12)¹³⁹. The prepared LEDs showed long half-lives of 5.2 h at room temperature and 2.2 h at 60 °C.

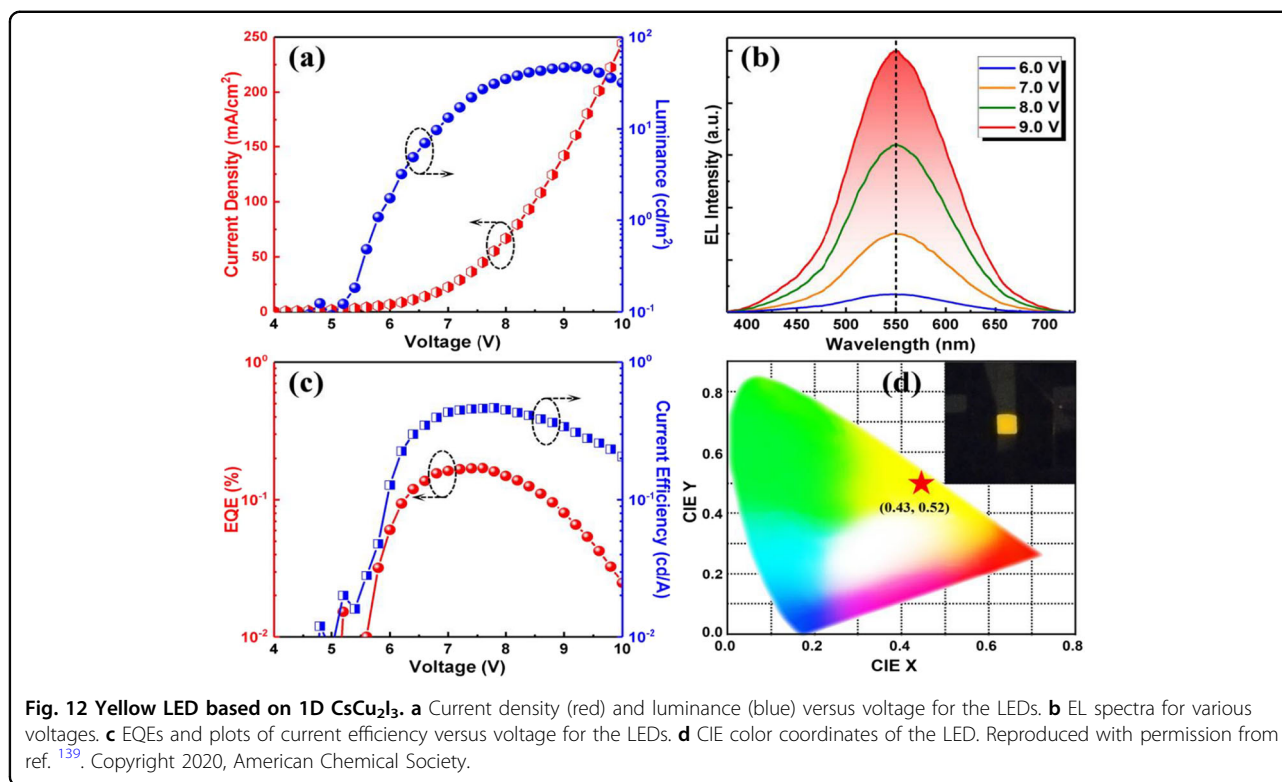
Photodetectors

High spectral selectivity is essential for PDs operated in different applications, including phototherapy, imaging,



fluorescence detection and biomedical sensing. In the work of Li et al., 1D anisotropic CsCu₂I₃ NWs were employed to assemble a polarization-sensitive UV PD on a flexible substrate, and the PD showed a large photocurrent-anisotropic ratio of 3.16¹⁴⁰. It showed superior photodetection ability with a responsivity of 32.3 A W⁻¹, a fast response/recovery speed of 6.94/214 μs, and a specific detectivity of 1.89 × 10¹² Jones. In addition, the device showed negligible degradation after 1000 bending cycles, suggesting good bending durability and flexibility. Additionally, Li et al. proposed a broadband and facet-dependent UV photodetector using 1D CsCu₂I₃ single-crystal microwires prepared via antisolvent engineering¹⁴¹. A higher on/off ratio was obtained with the {010} crystal plane because of the higher electron density and stronger confinement. Similarly, Yang et al. synthesized CsCu₂I₃ with a high exciton binding energy and a high PLQY of ~105 meV and 12.3%, respectively¹⁴². They developed a deep UV photodetector that exhibited nearly no response to visible light at 405 nm but was sensitive to 265 and 365 nm UV illumination. A high $I_{\text{light}}/I_{\text{dark}}$ ratio of 22 and excellent reproducibility was obtained for

265 nm illumination. Furthermore, the EQE, specific detectivity, and responsivity were as high as 10.3%, 1.2 × 10¹¹ Jones, and 22.1 mA/W, respectively. In another study, 1D Rb₂CuBr₃ single-crystal microwires were prepared with an optical band gap of 3.83 eV and good UV absorption¹⁴³. The as-prepared device displayed excellent UV detection of 265-nm light with a specific detectivity, responsivity, and response/recovery time of 1.23 × 10¹¹ Jones, 113.64 mA W⁻¹, and 69.31/87.55 ms, respectively (Fig. 13)¹⁴³. Moreover, long-term stability was observed during 2 weeks of storage in ambient air without encapsulation. In another study, Liu et al. obtained 1D N,N'-dimethylethylenediamine (DME) lead bromide via an antisolvent-assisted solution process¹⁴⁴. They used a temperature-dependent charge mobility measurement based on space charge limited current (SCLC) characterization to obtain a mobility of 4.51 cm²/Vs. A UV PD based on a 1D (DME)PbBr₄ single crystal displayed a photoresponsivity of 132.3 A W⁻¹. Overall, all-inorganic Cu(I)-based metal halides show great potential for producing low-cost, high-performance UV PDs.



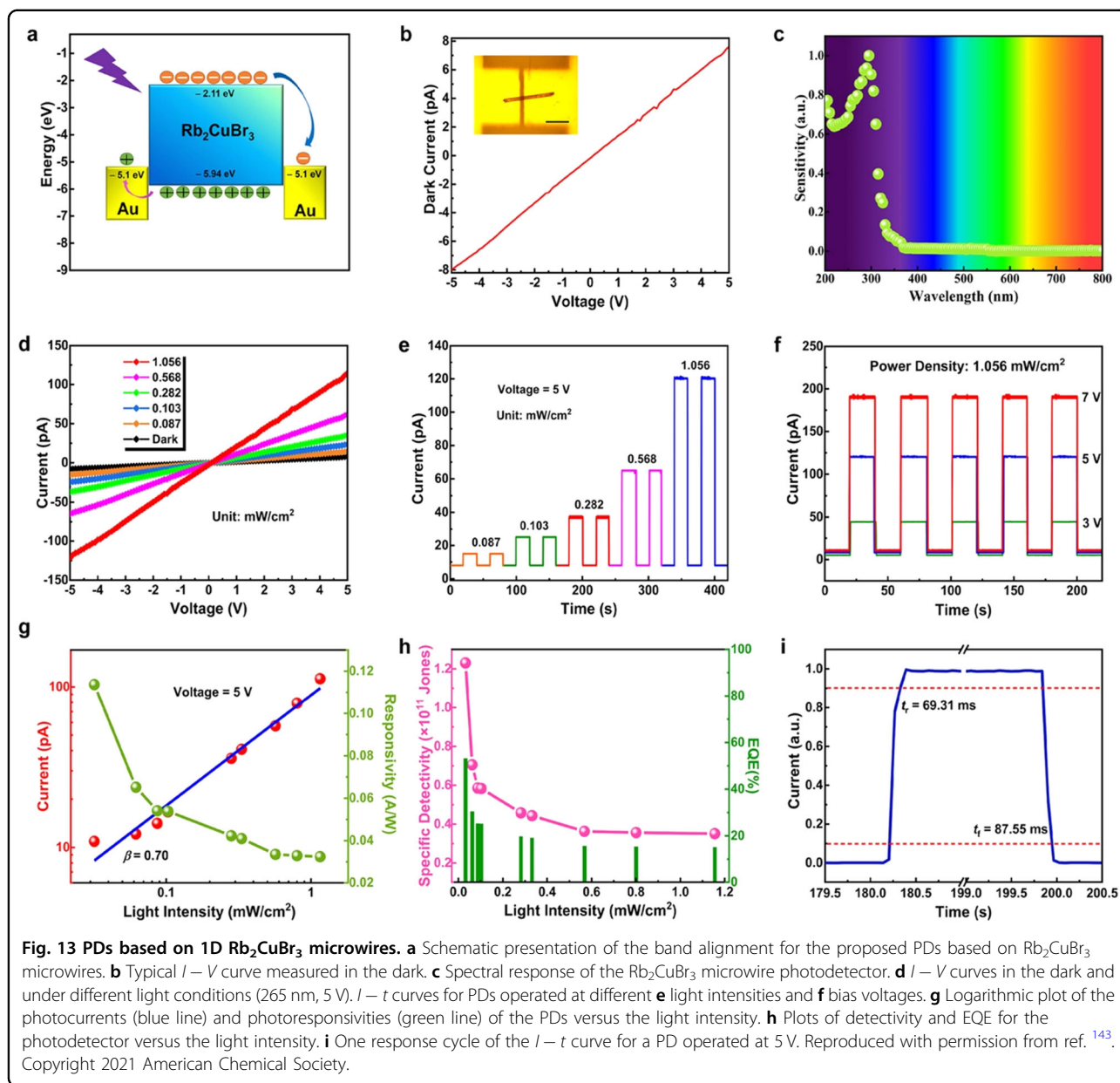
Zhang et al. designed and prepared a 1D perovskite single crystal in which the PbI₄²⁻ octahedra were caged by N,N'-dimethyl-1,2-ethanediamine (DMEDA) organic chains¹⁴⁵. Because of the absence of grain boundaries, ion migration was suppressed via the quantum size effect in a single crystal with a low trap state density. Thus, 1D MHP single-crystal photodetectors displayed hysteresis-free I–V curves. In addition, the photodetectors presented good stability, retaining 85% of their original photocurrent after 3 months of ambient storage.

In addition to UV light, circularly polarized light (CPL) was detected by chiral 1D perovskites, which were prepared from chiral cations with R- or S-configurations. Chen et al. prepared a chiral 1D (R- and S- α -PEA)PbI₃ film for CPL detection and obtained a maximum response of 0.12 A W⁻¹ at 395 nm¹⁴⁶. Due to the efficient charge transport in the inorganic frameworks and the sensitive absorption of the organic cations, the device displayed a detectivity of 7.1 \times 10¹¹ Jones. However, it showed a much lower dissymmetry factor (0.1) than other chiral CPL detectors, such as plasmonic metamaterials (1.09). To improve the circular dichroism (CD) of the chiral perovskites, Ishii and coworkers fabricated 1D perovskite-based CPL photodiodes from the chiral organic cations (R/S)-(1-(1-naphthyl)ethylammonium) [(R/S)-1-NEA]¹⁴⁷. They obtained a champion CD of 3000 mdeg among the reported perovskite systems. Zhao et al. constructed chiral 1D perovskite microwire arrays with pure (010)-

orientations by using a capillary-bridge-manipulation approach¹⁴⁸. Using the synergistic effect of the uniform crystallographic orientation and high crystallinity, efficient CPL photodetectors were prepared and showed a maximum anisotropy factor and detectivity of 0.23 and 2.2 \times 10¹¹ Jones, respectively. Moreover, the microwire-array-based CPL photodetectors displayed excellent environmental stability for 30 days under ambient conditions.

Other applications

A scintillator based on 1D Rb₂CuBr₃, which exhibited intense violet emission and a PLQY of \sim 98.6%, was developed for radiation detection¹⁴⁹. In combination with the STE-induced Stokes shift, the near-unity PLQY provided an extremely high radio-luminescence light yield of \sim 91056 photons per MeV, which was comparable to those of commercial scintillators. However, the radioactive nature of Rb raises environmental concerns. Alternatively, X-ray scintillators based on 1D K₂CuBr₃, which shows violet emission at 391 nm and a PLQY of 87%, were proposed¹⁵⁰. The resulting light yield (23806 photons per MeV) fell within the range for typical scintillators. Furthermore, the potassium-based 1D hybrid scintillator is environmentally friendly, and this expands the range of practical applications. Zhang and his coworkers developed lead-free 1D Rb₂AgCl₃ crystals as an efficient scintillator material exhibiting bright-orange emission at 580 nm and



a QY of 60.0%¹⁵¹. When the crystals were excited with X-rays, a fast scintillation decay time of 9.5 ns was obtained along with a light yield of 18300 photons MeV^{-1} . Furthermore, the ratio of light yield to decay time reached 1926 photons $\text{MeV}^{-1} \text{ns}^{-1}$, which exceeded the ratios for commercial scintillators.

Unlike the 3D trigonal black phase FAPbI_3 ($\alpha\text{-FAPbI}_3$), the yellow phase FAPbI_3 ($\delta\text{-FAPbI}_3$) adopts a 1D hexagonal crystal structure with good environmental and thermal stability. Based on the reduced structural dimensionality, researchers have explored applications other than photovoltaics. Park's group developed 1D and 3D FAPbI_3 via the Lewis acid-base adduct method and investigated the RS performance of the $\text{Ag}/\text{FAPbI}_3/\text{Pt}$

devices¹⁵². $\delta\text{-FAPbI}_3$ was formed when the annealing temperature was lower than 125°C , and $\alpha\text{-FAPbI}_3$ was generated at temperatures above 150°C . Both FAPbI_3 phases could be set from high-resistance state (HRS) to low-resistance state (LRS). However, failure of switching from LRS to HRS was observed for 3D $\alpha\text{-FAPbI}_3$, while the 1D $\delta\text{-FAPbI}_3$ devices worked well. DFT calculations revealed that the barrier for migration of the iodine cluster along the c -axis (0.48 eV) was smaller than that for the ab -plane (0.9 eV), which made the 3D isotropic $\alpha\text{-FAPbI}_3$ more stable than the 1D anisotropic $\delta\text{-FAPbI}_3$ and led to difficult filament rupture. The final 1D $\delta\text{-FAPbI}_3$ -based device demonstrated good endurance for more than 1200 cycles and a retention time of over 3000 s. These

results showed how structural dimensionality affects the formation/rupture of halide filaments in memory devices. In another study, a 1D halide perovskite, $(\text{NH} = \text{CINH}_3)_3\text{PbI}_5$ ($(\text{IFA})_3\text{PbI}_5$), was used in an RS device with the structure ITO/ $(\text{IFA})_3\text{PbI}_5/\text{Au}$ ¹⁵³. This device showed ultralow power consumption of 0.2 mW and a small set voltage of 0.2 V, which resulted from the low conductivity and wide bandgap (~ 3.0 eV) of the 1D material. This work provides the possibility of developing 1D molecular MHP-based low-power memory devices and other advanced optoelectronic applications.

Summary and future prospects

In this review, we highlighted recent advances made with both morphological- and molecular-level 1D MHPs during the past several years, including material syntheses, composition control, tuning of the properties, understanding of the fundamental mechanisms, and optoelectronic applications. Morphological and molecular level 1D MHPs have different merits from the perspective of optoelectronic applications. Since MHP NWs and NRs possess 1D crystal channels at the morphological level (dozens to a hundred nanometers in diameter), they usually present better electronic and carrier transport properties than molecular-level 1D MHPs, which contain 1D electronic connections at the molecular level (a few angstroms in diameter). On the other hand, molecular-level 1D MHPs often exhibit better stability when organic cations are used to isolate the molecular halide hybrid structures into 1D channels. Based on these distinct characteristics, morphological 1D MHPs alone have demonstrated high PCEs in solar cell applications⁷⁵, while molecular 1D MHPs were usually combined with 3D MHPs to generate 1D/3D structures that are useful for defect passivation and device stability¹³³. Furthermore, due to the presence of unique STEs, appropriately designed molecular 1D MHPs are suitable for upconversion lighting applications. For instance, as a consequence of the strong STE interactions, molecular-level 1D Rb_2CuCl_3 achieved a very high PLQY of $\sim 100\%$ ¹⁵⁴, which was much higher than those of morphological-level 1D MHPs. The range of organic cations available for molecular 1D MHPs also endows them with distinct optoelectronic properties for many applications¹⁵⁵. As an example, the use of chiral organic cations in molecular 1D MHPs has enabled interesting utility in detecting circularly polarized light¹⁴⁶. On the other hand, the 1D morphologies of MHP NWs and NRs, with sizes ranging from dozen of nanometers to wavelength scales, make them suitable for use in waveguides, metasurfaces, and linearly polarized light detection. Despite extensive effort, there is still ample room for developing novel 1D MHPs, investigating the principles between their structures, properties, and performance, and exploring novel

applications. It is essential to determine general principles for designing and preparing high-quality and stable MHPs with controlled compositions, structures, and dimensionalities. There are major challenges and future prospects that need to be addressed in order to advance this field, including but not limited to the following:

1. 1D morphological MHPs usually show stronger light absorption and better stability in various applications due to their geometric characteristics. In particular, 1D MHP NWs with longer lifetimes of the photogenerated carriers, lower recombination rates, fewer defects and lower trap densities display great potential for use in solar cells. In the absence of a template, vertical growth of the 1D MHP NWs on a substrate would remarkably improve the PCEs of solar cells. For lasers, 1D MHPs have shown better performance than granular films due to the high optical gains and quantum confinement under excitation. In addition, higher sensitivity and lower carrier recombination rates could enable light detection capability exceeding those of other semiconductors, which would be useful in photodetectors. Orderly NW or NR arrays have exhibited superior stability, and more effort should be expended. A thorough understanding of the relationships among the preparation processes, structures (morphology), and properties, together with the well-controlled morphologies, would make 1D morphological MHPs promising candidates for use in photovoltaics and other optoelectronics.

2. Current development of 1D molecular MHPs largely relies on trial-and-error synthetic methods. Although considerable effort has been devoted to investigating the photophysical processes and optoelectronic properties of 1D MHPs, the complexity of the excited state kinetics and dynamics and the various defect characteristics, densities, and positions in the bandgap require reliable approaches allowing precise regulation of the crystallinities, structures, and sizes of 1D MHPs. It will be of great interest to explore novel halide polyhedra, such as pyramids and tetrahedra, for use as the building units of 1D network chains. More synthetic methods and effective computational models must be developed to predict how bulk crystals are assembled from the organic and inorganic components and to better understand fundamental mechanisms, including how the interactions between organic and inorganic ions affect the photophysical properties. In addition, the toxicity of Pb, which is widely used in 1D MHPs, is harmful to the environment. Therefore, it is imperative to develop efficient and stable lead-free MHPs, such as Sn-, Ge-, Sb-, and Bi-based MHPs.

3. Based on their high crystallinities and PLQYs, excellent charge carrier mobilities, and low defect rates, 1D MHPs are among the most promising candidates for use in optoelectronic devices, including PDs, transistors,

and lasers. However, applications based on these materials cannot be widely explored because of the incomplete surface coverage that severely affects device performance and reproducibility. Moreover, the mechanisms for other stimulation methods used with 1D MHP-based devices, such as those for polarized light, pressure, temperature, and magnetic fields, have not been well investigated. In addition, we should explore other potential applications, including magnetic storage, solar concentrators, phonon transport, waveguides, and scintillators.

4. Because of their isolated structures, 1D MHPs exhibit ambient stability superior to those of their 3D counterparts. However, they are still not sufficiently stable to meet the requirements for practical application. To understand how these 1D MHPs degrade, further studies are essential for identifying the mechanisms for degradation by moisture, oxygen, UV light, and heat. The photostabilities of the 1D MHPs might be influenced by dissociation and reformation of metal halide bonds. More experimental and theoretical studies should be performed to improve the stability of the 1D structures based on large and rigid organic components or cross-linked organic components. In addition, increasing the ionic interactions between anions and cations in 1D MHPs would provide a better understanding of the intrinsic stabilities of the 1D MHPs.

5. Construction of multidimensional 1D/3D perovskite composites has proven to be effective in preparing efficient and stable photovoltaic devices, especially for solar cell applications. The optoelectronic capabilities of many 1D MHP-based devices are still limited by tradeoffs involving transparency and light harvesting, efficiency and stability, performance, and cost. We believe that rapid evolution of 1D/3D MHPs will create more win-win opportunities in the future. Although many exciting results have been obtained, the intrinsic growth mechanisms must be revealed. It is also essential to determine how the 1D MHPs affect the crystallization kinetics, phase purities, and orientations of 3D bulk perovskites and how this, in turn, affects photocarrier transport, recombination processes, and the concentrations of defect states. Investigations of the structure-performance relationships affecting 1D/3D perovskite composites, their photovoltaic capabilities, and stabilities could provide a theoretical basis for optimizing perovskite devices and promoting the industrialization of perovskite-based optoelectronic technologies.

In general, the range of accessible A-site cations used in molecular 1D MHPs provides a substantial engineering platform with which to seek novel materials with diverse electronic and photophysical properties. Although significant progress has been made, research on molecular 1D MHPs is still at the preliminary stage, and many open questions remain unanswered. For morphological 1D

MHPs, it is critical to develop novel techniques for fabricating large-area perovskite films with the controlled alignments of the 1D morphologies. Controlling the nucleation rate with a proper understanding of the chemical kinetics and thermodynamics of the growth system is critical for harnessing the full potential of these materials in various optoelectronic applications. Last but not least, many hidden properties and unexplored uses of these promising materials remain to be discovered. We hope this review will attract more research interest and provide insightful perspectives for future explorations of 1D MHPs.

Acknowledgements

This work is supported by the Scientific Research Startup Fund for Shenzhen High-Caliber Personnel of Shenzhen Polytechnic, Nos. 6022310038k and 6022310049k. The financial support from the National Natural Science Foundation of China (62004129; 22005202) and Shenzhen Science and Technology Innovation Commission (Project No. JCYJ20200109105003940) is gratefully acknowledged, and this work was also supported by the PostDoctoral Foundation Project of Shenzhen Polytechnic 6021330007 K.

Author details

¹Hoffmann Institute of Advanced Materials, Postdoctoral Innovation Practice Base, Shenzhen Polytechnic, Nanshan District, Shenzhen 518055, P. R. China. ²School of Materials Science and Engineering, University of New South Wales (UNSW), Sydney, NSW 2052, Australia. ³International Collaborative Laboratory of 2D Materials for Optoelectronics Science and Technology of Ministry of Education, Institute of Microscale Optoelectronics, Shenzhen University, Shenzhen 518060, China. ⁴Department of Applied Physics, The Hong Kong Polytechnic University, Kowloon, Hong Kong, China

Author contributions

D.D. and C.G. contributed equally to this work, collected the literature, and wrote the manuscript. M.Z.R., C.-H.L., Y.S., and H.L. contributed to the review and editing of the paper. H.H. and T.W. conceived the theme and supervised this review. All authors read and approved the manuscript.

Competing interests

The authors declare no competing interests.

Publisher's note

Springer Nature remains neutral with regard to jurisdictional claims in published maps and institutional affiliations.

Received: 23 November 2022 Revised: 18 January 2023 Accepted: 20 January 2023.

Published online: 24 February 2023

References

1. Wang, F. et al. Recent progress of scalable perovskite solar cells and modules. *Energy Rev.* **1**, 100010 (2022).
2. Uzurano, G., Kuwahara, N., Saito, T., Fujii, A. & Ozaki, M. Orientation control of 2D perovskite in 2D/3D heterostructure by templated growth on 3D perovskite. *ACS Mater. Lett.* **4**, 378–384 (2022).
3. Burn, P. L. & Meredith, P. The rise of the perovskites: the future of low cost solar photovoltaics? *NPG Asia Mater.* **6**, e79–e79 (2014).
4. Huang, H. et al. Colloidal lead halide perovskite nanocrystals: synthesis, optical properties and applications. *NPG Asia Mater.* **8**, e328–e328 (2016).
5. Fu, Y. et al. Metal halide perovskite nanostructures for optoelectronic applications and the study of physical properties. *Nat. Rev. Mater.* **4**, 169–188 (2019).
6. Ge, C., Fang, Q., Lin, H. & Hu, H. Review on blue perovskite light-emitting diodes: recent advances and future prospects. *Front. Mater.* **8**, 1–7 (2021).

7. Dhifaoui, H. et al. An approach to quantify the negative capacitance features in a triple-cation based perovskite solar cells. *Adv. Mater. Interfaces* **8**, 2101002 (2021).
8. Zhou, C. et al. Low dimensional metal halide perovskites and hybrids. *Mater. Sci. Eng. R. Rep.* **137**, 38–65 (2019).
9. Hu, L. et al. Valence-regulated metal doping of mixed-halide perovskites to modulate phase segregation and solar cell performance. *ACS Energy Lett.* **7**, 4150–4160 (2022).
10. Qiao, W.-C. et al. Formamidinium lead triiodide perovskites with improved structural stabilities and photovoltaic properties obtained by ultratrace dimethylamine substitution. *NPG Asia Mater.* **14**, 49 (2022).
11. Zhang, J. et al. Low-dimensional halide perovskites and their advanced optoelectronic applications. *Nano-Micro Lett.* **9**, 1–26 (2017).
12. Lin, H., Zhou, C., Tian, Y., Siegrist, T. & Ma, B. Low-dimensional organometal halide perovskites. *ACS Energy Lett.* **3**, 54–62 (2018).
13. Han, Y., Yue, S. & Cui, B. Low-dimensional metal halide perovskite crystal materials: structure strategies and luminescence applications. *Adv. Sci.* **8**, 2004805 (2021).
14. Kojima, A., Teshima, K., Shirai, Y. & Miyasaka, T. Organometal halide perovskites as visible-light sensitizers for photovoltaic cells. *J. Am. Chem. Soc.* **131**, 6050–6051 (2009).
15. Jia, P. et al. Recent advances in flexible perovskite light-emitting diodes. *Adv. Mater. Interfaces* **8**, 2100441 (2021).
16. Liang, X. et al. The role of ionic liquids in performance enhancement of two-step perovskite photovoltaics. *Sol. RRL* **7**, 2200856 (2022).
17. Wang, F. et al. In-depth understanding of ionic liquid assisted perovskite film formation mechanism for two-step perovskite photovoltaics. *J. Energy Chem.* **73**, 599–606 (2022).
18. Lin, K. et al. Perovskite light-emitting diodes with external quantum efficiency exceeding 20 per cent. *Nature* **562**, 245–248 (2018).
19. Hassan, Y. et al. Ligand-engineered bandgap stability in mixed-halide perovskite LEDs. *Nature* **591**, 72–77 (2021).
20. Yu, H. et al. Waterproof cesium lead bromide perovskite lasers and their applications in solution. *ACS Nano* **14**, 552–558 (2020).
21. Chen, S., Zhang, C., Lee, J., Han, J. & Nurmikko, A. High-Q, low-threshold monolithic perovskite thin-film vertical-cavity lasers. *Adv. Mater.* **29**, 1604781 (2017).
22. Liu, Y. et al. Low-temperature-gradient crystallization for multi-inch high-quality perovskite single crystals for record performance photodetectors. *Mater. Today* **22**, 67–75 (2019).
23. Wang, M., Sun, H., Cao, F., Tian, W. & Li, L. Moisture-triggered self-healing flexible perovskite photodetectors with excellent mechanical stability. *Adv. Mater.* **33**, 2100625 (2021).
24. Kang, K. et al. High-performance solution-processed organo-metal halide perovskite unipolar resistive memory devices in a cross-bar array structure. *Adv. Mater.* **31**, 1804841 (2019).
25. Gu, C. & Lee, J.-S. Flexible hybrid organic–inorganic perovskite memory. *ACS Nano* **10**, 5413–5418 (2016).
26. She, X.-J. et al. A solvent-based surface cleaning and passivation technique for suppressing ionic defects in high-mobility perovskite field-effect transistors. *Nat. Electron.* **3**, 694–703 (2020).
27. Zhou, X. et al. Dimethylammonium cation-induced 1D/3D heterostructure for efficient and stable perovskite solar cells. *Molecules* **27**, 7566 (2022).
28. Ge, C., Xue, Y. Z. B., Li, L., Tang, B. & Hu, H. Recent progress in 2D/3D multidimensional metal halide perovskites solar cells. *Front. Mater.* **7**, 601179 (2020).
29. Qiu, T. et al. Recent advances in one-dimensional halide perovskites for optoelectronic applications. *Nanoscale* **10**, 20963–20989 (2018).
30. Zhang, Y. et al. Synthesis, properties, and optical applications of low-dimensional perovskites. *Chem. Commun.* **52**, 13637–13655 (2016).
31. Hu, H. et al. Perovskite quantum wells formation mechanism for stable efficient perovskite photovoltaics—a real-time phase-transition study. *Adv. Mater.* **33**, 2006238 (2021).
32. Zhu, P. & Zhu, J. Low-dimensional metal halide perovskites and related optoelectronic applications. *InfoMat* **2**, 341–378 (2020).
33. Huang, J., Lai, M., Lin, J. & Yang, P. Rich chemistry in inorganic halide perovskite nanostructures. *Adv. Mater.* **30**, 1802856 (2018).
34. Misra, R. K., Cohen, B.-E., Iagher, L. & Etgar, L. Low-dimensional organic-inorganic halide perovskite: structure, properties, and applications. *ChemSusChem* **10**, 3712–3721 (2017).
35. Mohammed, O. F. Outstanding challenges of zero-dimensional perovskite materials. *J. Phys. Chem. Lett.* **10**, 5886–5888 (2019).
36. Mao, L., Stoumpos, C. C. & Kanatzidis, M. G. Two-dimensional hybrid halide perovskites: principles and promises. *J. Am. Chem. Soc.* **141**, 1171–1190 (2019).
37. Zhang, L., Liu, Y., Yang, Z. & Liu, S. F. Two dimensional metal halide perovskites: Promising candidates for light-emitting diodes. *J. Energy Chem.* **37**, 97–110 (2019).
38. Stranks, S. D. et al. Electron-hole diffusion lengths exceeding 1 micrometer in an organometal trihalide perovskite absorber. *Science* **342**, 341–344 (2013).
39. Xiao, R. et al. Photocurrent mapping in single-crystal methylammonium lead iodide perovskite nanostructures. *Nano Lett.* **16**, 7710–7717 (2016).
40. Deng, W. et al. Ultrahigh-responsivity photodetectors from perovskite nanowire arrays for sequentially tunable spectral measurement. *Nano Lett.* **17**, 2482–2489 (2017).
41. Horváth, E. et al. Nanowires of methylammonium lead iodide (CH₃NH₃PbI₃) prepared by low temperature solution-mediated crystallization. *Nano Lett.* **14**, 6761–6766 (2014).
42. Zhu, H. et al. Lead halide perovskite nanowire lasers with low lasing thresholds and high quality factors. *Nat. Mater.* **14**, 636–642 (2015).
43. Fu, Y. et al. Nanowire lasers of formamidinium lead halide perovskites and their stabilized alloys with improved stability. *Nano Lett.* **16**, 1000–1008 (2016).
44. Wong, A. B. et al. Growth and anion exchange conversion of CH₃NH₃PbX₃ nanorod arrays for light-emitting diodes. *Nano Lett.* **15**, 5519–5524 (2015).
45. Fu, Y. et al. Broad wavelength tunable robust lasing from single-crystal nanowires of cesium lead halide perovskites (CsPbX₃, X = Cl, Br, I). *ACS Nano* **10**, 7963–7972 (2016).
46. Huang, C.-Y. et al. Inorganic halide perovskite quantum dots: a versatile nanomaterial platform for electronic applications. *Nano-Micro Lett.* **15**, 16 (2023).
47. Meng, F., Morin, S. A., Forticaux, A. & Jin, S. Screw dislocation driven growth of nanomaterials. *Acc. Chem. Res.* **46**, 1616–1626 (2013).
48. Ha, S. T. et al. Synthesis of organic-inorganic lead halide perovskite nanoplatelets: towards high-performance perovskite solar cells and optoelectronic devices. *Adv. Opt. Mater.* **2**, 838–844 (2014).
49. Xing, J. et al. Vapor phase synthesis of organometal halide perovskite nanowires for tunable room-temperature nanolasers. *Nano Lett.* **15**, 4571–4577 (2015).
50. Chen, J. et al. Vapor-phase epitaxial growth of aligned nanowire networks of cesium lead halide perovskites (CsPbX₃, X = Cl, Br, I). *Nano Lett.* **17**, 460–466 (2017).
51. Zhou, H. et al. Vapor growth and tunable lasing of band gap engineered cesium lead halide perovskite micro/nanorods with triangular cross section. *ACS Nano* **11**, 1189–1195 (2017).
52. Zhang, D., Eaton, S. W., Yu, Y., Dou, L. & Yang, P. Solution-phase synthesis of cesium lead halide perovskite nanowires. *J. Am. Chem. Soc.* **137**, 9230–9233 (2015).
53. Liu, W. et al. General strategy for rapid production of low-dimensional all-inorganic CsPbBr₃ perovskite nanocrystals with controlled dimensionalities and sizes. *Inorg. Chem.* **57**, 1598–1603 (2018).
54. Tang, X. et al. All-inorganic perovskite CsPb(Br/I)₃ nanorods for optoelectronic application. *Nanoscale* **8**, 15158–15161 (2016).
55. Wang, S. et al. Stable, strongly emitting cesium lead bromide perovskite nanorods with high optical gain enabled by an intermediate monomer reservoir synthetic strategy. *Nano Lett.* **19**, 6315–6322 (2019).
56. Tailor, N. K. et al. Advances in lead-free perovskite single crystals: fundamentals and applications. *ACS Mater. Lett.* **3**, 1025–1080 (2021).
57. Chen, L.-J., Lee, C.-R., Chuang, Y.-J., Wu, Z.-H. & Chen, C. Synthesis and optical properties of lead-free cesium tin halide perovskite quantum rods with high-performance solar cell application. *J. Phys. Chem. Lett.* **7**, 5028–5035 (2016).
58. Wang, A. et al. Controlled synthesis of lead-free and stable perovskite derivative Cs₂SnI₆ nanocrystals via a facile hot-injection process. *Chem. Mater.* **28**, 8132–8140 (2016).
59. Bu, W., Chen, Z., Chen, F. & Shi, J. Oleic acid/oleylamine cooperative-controlled crystallization mechanism for monodisperse tetragonal bipyramid NaLa(MoO₄)₂ nanocrystals. *J. Phys. Chem. C* **113**, 12176–12185 (2009).
60. Li, Y., Liu, J., Wang, Y. & Wang, Z. L. Preparation of monodispersed Fe—Mo nanoparticles as the catalyst for CVD synthesis of carbon nanotubes. *Chem. Mater.* **13**, 1008–1014 (2001).

61. Fu, Y. et al. Solution growth of single crystal methylammonium lead halide perovskite nanostructures for optoelectronic and photovoltaic applications. *J. Am. Chem. Soc.* **137**, 5810–5818 (2015).
62. Kwon, H.-C. et al. Investigating recombination and charge carrier dynamics in a one-dimensional nanopillared perovskite absorber. *ACS Nano* **12**, 4233–4245 (2018).
63. Ashley, M. J. et al. Templated synthesis of uniform perovskite nanowire arrays. *J. Am. Chem. Soc.* **138**, 10096–10099 (2016).
64. Oener, S. Z. et al. Perovskite nanowire extrusion. *Nano Lett.* **17**, 6557–6563 (2017).
65. Gu, L. et al. 3D arrays of 1024-pixel image sensors based on lead halide perovskite nanowires. *Adv. Mater.* **28**, 9713–9721 (2016).
66. Waleed, A. et al. Lead-free perovskite nanowire array photodetectors with drastically improved stability in nanoengineering templates. *Nano Lett.* **17**, 523–530 (2017).
67. Yen, H.-J. et al. Large grained perovskite solar cells derived from single-crystal perovskite powders with enhanced ambient stability. *ACS Appl. Mater. Interfaces* **8**, 14513–14520 (2016).
68. Li, D. et al. Humidity-induced grain boundaries in MAPbI₃ perovskite films. *J. Phys. Chem. C* **120**, 6363–6368 (2016).
69. Zhu, F. et al. Shape evolution and single particle luminescence of organo-metal halide perovskite nanocrystals. *ACS Nano* **9**, 2948–2959 (2015).
70. Liu, Y. et al. Room temperature colloidal synthesis of CsPbBr₃ nanowires with tunable length, width and composition. *J. Mater. Chem. C* **6**, 7797–7802 (2018).
71. Imran, M. et al. Colloidal synthesis of strongly fluorescent CsPbBr₃ nanowires with width tunable down to the quantum confinement regime. *Chem. Mater.* **28**, 6450–6454 (2016).
72. Yang, H., Cai, T., Dube, L., Hills-Kimball, K. & Chen, O. Synthesis of ultrathin perovskite nanowires via a postsynthetic transformation reaction of zero-dimensional perovskite nanocrystals. *Cryst. Growth Des.* **21**, 1924–1930 (2021).
73. Min, H. et al. Perovskite solar cells with atomically coherent interlayers on SnO₂ electrodes. *Nature* **598**, 444–450 (2021).
74. Im, J.-H. et al. Nanowire perovskite solar cell. *Nano Lett.* **15**, 2120–2126 (2015).
75. Chang, C.-Y., Tsai, B.-C., Lin, M.-Z., Huang, Y.-C. & Tsao, C.-S. An integrated approach towards the fabrication of highly efficient and long-term stable perovskite nanowire solar cells. *J. Mater. Chem. A* **5**, 22824–22833 (2017).
76. Xiao, K. et al. Amine treatment induced perovskite nanowire network in perovskite solar cells: efficient surface passivation and carrier transport. *Nanotechnology* **29**, 065401 (2018).
77. Liao, J.-F. et al. Inorganic cesium lead halide CsPbX₃ nanowires for long-term stable solar cells. *Sci. China Mater.* **60**, 285–294 (2017).
78. Lin, C.-H. et al. Designed growth and patterning of perovskite nanowires for lasing and wide color gamut phosphors with long-term stability. *Nano Energy* **73**, 104801 (2020).
79. Park, K. et al. Light-matter interactions in cesium lead halide perovskite nanowire lasers. *J. Phys. Chem. Lett.* **7**, 3703–3710 (2016).
80. Sum, T. C., Chen, S., Xing, G., Liu, X. & Wu, B. Energetics and dynamics in organic-inorganic halide perovskite photovoltaics and light emitters. *Nanotechnology* **26**, 342001 (2015).
81. Binek, A., Hanusch, F. C., Docampo, P. & Bein, T. Stabilization of the trigonal high-temperature phase of formamidinium lead iodide. *J. Phys. Chem. Lett.* **6**, 1249–1253 (2015).
82. Eperon, G. E. et al. Formamidinium lead trihalide: a broadly tunable perovskite for efficient planar heterojunction solar cells. *Energy Environ. Sci.* **7**, 982 (2014).
83. Li, Z., Liu, X., Zuo, C., Yang, W. & Fang, X. Supersaturation-controlled growth of monolithically integrated lead-free halide perovskite single-crystalline thin film for high-sensitivity photodetectors. *Adv. Mater.* **33**, 2103010 (2021).
84. Li, S., Zhang, Y., Yang, W., Liu, H. & Fang, X. 2D perovskite Sr₂Nb₃O₁₀ for high-performance UV photodetectors. *Adv. Mater.* **32**, 1905443 (2020).
85. Zhuo, S., Zhang, J., Shi, Y., Huang, Y. & Zhang, B. Self-template-directed synthesis of porous perovskite nanowires at room temperature for high-performance visible-light photodetectors. *Angew. Chem.* **127**, 5785–5788 (2015).
86. Deng, H. et al. Flexible and semitransparent organolead triiodide perovskite network photodetector arrays with high stability. *Nano Lett.* **15**, 7963–7969 (2015).
87. Wang, Y. et al. Photon transport in one-dimensional incommensurately epitaxial CsPbX₃ arrays. *Nano Lett.* **16**, 7974–7981 (2016).
88. Han, M. et al. Controllable growth of lead-free all-inorganic perovskite nanowire array with fast and stable near-infrared photodetection. *J. Phys. Chem. C* **123**, 17566–17573 (2019).
89. Deng, W. et al. Aligned single-crystalline perovskite microwire arrays for high-performance flexible image sensors with long-term stability. *Adv. Mater.* **28**, 2201–2208 (2016).
90. Wang, J., Gudiksen, M. S., Duan, X., Cui, Y. & Lieber, C. M. Highly polarized photoluminescence and photodetection from single indium phosphide nanowires. *Science* **293**, 1455–1457 (2001).
91. Lin, C. et al. Giant optical anisotropy of perovskite nanowire array films. *Adv. Funct. Mater.* **30**, 1909275 (2020).
92. Gao, L. et al. Passivated single-crystalline CH₃NH₃PbI₃ nanowire photodetector with high detectivity and polarization sensitivity. *Nano Lett.* **16**, 7446–7454 (2016).
93. Feng, J. et al. Crystallographically aligned perovskite structures for high-performance polarization-sensitive photodetectors. *Adv. Mater.* **29**, 1605993 (2017).
94. Fang, Y., Dong, Q., Shao, Y., Yuan, Y. & Huang, J. Highly narrowband perovskite single-crystal photodetectors enabled by surface-charge recombination. *Nat. Photonics* **9**, 679–686 (2015).
95. Shoaib, M. et al. Directional growth of ultralong CsPbBr₃ perovskite nanowires for high-performance photodetectors. *J. Am. Chem. Soc.* **139**, 15592–15595 (2017).
96. Zhang, D. et al. Metal halide perovskite nanowires: synthesis, integration, properties, and applications in optoelectronics. *Adv. Energy Mater.* <https://doi.org/10.3390/nano13030419> (2022).
97. Guo, J. et al. Pb²⁺ doped CsCdBr₃ perovskite nanorods for pure-blue light-emitting diodes. *Chem. Eng. J.* **427**, 131010 (2022).
98. Bi, C. et al. Self-assembled perovskite nanowire clusters for high luminance red light-emitting diodes. *Adv. Funct. Mater.* **30**, 2005990 (2020).
99. Wang, H. P. et al. Low-dimensional metal halide perovskite photodetectors. *Adv. Mater.* **33**, 2003309 (2021).
100. Chen, Y. et al. Hybrid field-effect transistors and photodetectors based on organic semiconductor and CsPbI₃ Perovskite nanorods bilayer structure. *Nano-Micro Lett.* **10**, 57 (2018).
101. Chen, P.-A. et al. Microfluidic solution-processed organic and perovskite nanowires fabricated for field-effect transistors and photodetectors. *J. Mater. Chem. C* **8**, 2353–2362 (2020).
102. Zhao, J. et al. Light-induced anomalous resistive switches based on individual organic-inorganic halide perovskite micro-/nanofibers. *Adv. Electron. Mater.* **4**, 1800206 (2018).
103. Poddar, S. et al. Down-scalable and ultra-fast memristors with ultra-high density three-dimensional arrays of perovskite quantum wires. *Nano Lett.* **21**, 5036–5044 (2021).
104. Rahaman, M. Z., Ge, S., Lin, C.-H., Cui, Y. & Wu, T. One-dimensional molecular metal halide materials: structures, properties, and applications. *Small Struct.* **2**, 2000062 (2021).
105. Yu, G. et al. One-dimensional organic-metal halide with highly efficient warm white-light emission and its moisture-induced structural transformation. *Chem. Mater.* **33**, 5668–5674 (2021).
106. Hong, K., Le, Q., Van, Kim, S. Y. & Jang, H. W. Low-dimensional halide perovskites: review and issues. *J. Mater. Chem. C* **6**, 2189–2209 (2018).
107. Ha, S. T., Su, R., Xing, J., Zhang, Q. & Xiong, Q. Metal halide perovskite nanomaterials: synthesis and applications. *Chem. Sci.* **8**, 2522–2536 (2017).
108. Mitzi, D. B., Wang, S., Feild, C. A., Chess, C. A. & Guloy, A. M. Conducting layered organic-inorganic halides containing <110>-oriented perovskite sheets. *Science* **267**, 1473–1476 (1995).
109. Wang, S., Mitzi, D. B., Feild, C. A. & Guloy, A. Synthesis and characterization of [NH₂C(=O)NH₂]₃Ml₅ (M = Sn, Pb): stereochemical activity in divalent tin and lead halides containing single <110> perovskite sheets. *J. Am. Chem. Soc.* **117**, 5297–5302 (1995).
110. Mao, L. et al. Structural diversity in white-light-emitting hybrid lead bromide perovskites. *J. Am. Chem. Soc.* **140**, 13078–13088 (2018).
111. Yuan, Z. et al. One-dimensional organic lead halide perovskites with efficient bluish white-light emission. *Nat. Commun.* **8**, 14051 (2017).
112. Wang, Y. et al. Reaching 90% photoluminescence quantum yield in one-dimensional metal halide C₄N₂H₁₄PbBr₄ by pressure-suppressed nonradiative loss. *J. Am. Chem. Soc.* **142**, 16001–16006 (2020).
113. Zhou, C. et al. Manganese-doped one-dimensional organic lead bromide perovskites with bright white emissions. *ACS Appl. Mater. Interfaces* **9**, 40446–40451 (2017).

114. Liu, Y. et al. Mechanism for tunable broadband white photoluminescence of one-dimensional $(\text{C}_4\text{N}_2\text{H}_{14})_2\text{Pb}_{1-x}\text{Mn}_x\text{Br}_4$ perovskite microcrystals. *J. Lumin.* **221**, 117045 (2020).
115. Wu, G. et al. A one-dimensional organic lead chloride hybrid with excitation-dependent broadband emissions. *ACS Energy Lett.* **3**, 1443–1449 (2018).
116. Li, D. et al. A one-dimensional dual emissive hybrid perovskite with flexibly tunable white-light emission. *J. Mater. Chem. C* **8**, 6710–6714 (2020).
117. Zhou, C. et al. Low-dimensional organic tin bromide perovskites and their photoinduced structural transformation. *Angew. Chem. Int. Ed.* **56**, 9018–9022 (2017).
118. Mousdis, G. A. et al. One-dimensional organic-inorganic hybrid materials based on antimony. *Eur. J. Inorg. Chem.* **2017**, 3401–3408 (2017).
119. Zhang, J. et al. A lead-free perovskite-like hybrid with above-room-temperature switching of quadratic nonlinear optical properties. *Chem. Commun.* **54**, 5614–5617 (2018).
120. Dammak, H., Triki, S., Mlayah, A., Abid, Y. & Feki, H. Structural, vibrational and optical properties of a new self assembled organic-inorganic nanowire crystal $(\text{C}_6\text{H}_{14}\text{N})_2[\text{BiBr}_5]$: a density functional theory approach. *J. Lumin.* **166**, 180–186 (2015).
121. Zhang, W. et al. $(\text{C}_6\text{H}_{13}\text{N})_2\text{BiI}_5$: a one-dimensional lead-free perovskite-derivative photoconductive light absorber. *Inorg. Chem.* **57**, 4239–4243 (2018).
122. Hu, Y.-Q. et al. Crystal and band-gap engineering of one-dimensional antimony/bismuth-based organic-inorganic hybrids. *Inorg. Chem.* **58**, 16346–16353 (2019).
123. Lin, H. et al. Bulk assembly of organic metal halide nanotubes. *Chem. Sci.* **8**, 8400–8404 (2017).
124. Hu, R. et al. Novel photoelectric material of perovskite-like $(\text{CH}_3)_3\text{SPbI}_3$ nanorod arrays with high stability. *J. Energy Chem.* **59**, 581–588 (2021).
125. Rahman, M. M., Ye Ge, C., Yoo, K. & Lee, J. J. Aqueous phase synthesis of trimethylsulfoxonium lead triiodide for moisture-stable perovskite solar cells. *Mater. Today Energy* **21**, 100803 (2021).
126. Chu, Z. et al. Emerging low-dimensional crystal structure of metal halide perovskite optoelectronic materials and devices. *Small Struct.* **2**, 2000133 (2021).
127. Ge, C. et al. Mixed dimensional perovskites heterostructure for highly efficient and stable perovskite solar cells. *Sol. RRL* **6**, 2100879 (2021).
128. Liu, J. et al. Synthesis and optical applications of low dimensional metal-halide perovskites. *Nanotechnology* **31**, 152002 (2020).
129. Bi, D. et al. High-performance perovskite solar cells with enhanced environmental stability based on amphiphile-modified $\text{CH}_3\text{NH}_3\text{PbI}_3$. *Adv. Mater.* **28**, 2910–2915 (2016).
130. Fan, J. et al. Thermodynamically self-healing 1D–3D hybrid perovskite solar cells. *Adv. Energy Mater.* **8**, 1703421 (2018).
131. Liu, P. et al. Lattice-matching structurally-stable 1D@3D perovskites toward highly efficient and stable solar cells. *Adv. Energy Mater.* **10**, 1903654 (2020).
132. Yu, S. et al. Hydrazinium cation mixed FAPbI_3 -based perovskite with 1D/3D hybrid dimension structure for efficient and stable solar cells. *Chem. Eng. J.* **403**, 125724 (2021).
133. Gao, L. et al. Improved environmental stability and solar cell efficiency of $(\text{MA,FA})\text{PbI}_3$ perovskite using a wide-band-gap 1D thiazolium lead iodide capping layer strategy. *ACS Energy Lett.* **4**, 1763–1769 (2019).
134. Xu, A. F. et al. Promoting thermodynamic and kinetic stabilities of FA-based perovskite by an in situ bilayer structure. *Nano Lett.* **20**, 3864–3871 (2020).
135. Yang, N. et al. An in situ cross-linked 1D/3D perovskite heterostructure improves the stability of hybrid perovskite solar cells for over 3000 h operation. *Energy Environ. Sci.* **13**, 4344–4352 (2020).
136. Kong, T. et al. Perovskite-templated formation of a 1D@3D perovskite structure toward highly efficient and stable perovskite solar cells. *Adv. Energy Mater.* **11**, 2101018 (2021).
137. Lin, R. et al. All-inorganic CsCu_2I_3 single crystal with high-PLQY ($\approx 15.7\%$) intrinsic white-light emission via strongly localized 1D excitonic recombination. *Adv. Mater.* **31**, 1905079 (2019).
138. Mo, X. et al. Highly-efficient all-inorganic lead-free 1D CsCu_2I_3 single crystal for white-light emitting diodes and UV photodetection. *Nano Energy* **81**, 105570 (2021).
139. Ma, Z. et al. Stable yellow light-emitting devices based on ternary copper halides with broadband emissive self-trapped excitons. *ACS Nano* **14**, 4475–4486 (2020).
140. Li, Y. et al. Solution-processed one-dimensional CsCu_2I_3 nanowires for polarization-sensitive and flexible ultraviolet photodetectors. *Mater. Horiz.* **7**, 1613–1622 (2020).
141. Li, Z. Z., Li, Z. Z., Shi, Z. & Fang, X. Facet-dependent, fast response, and broadband photodetector based on highly stable all-inorganic CsCu_2I_3 single crystal with 1D electronic structure. *Adv. Funct. Mater.* **30**, 2002634 (2020).
142. Yang, J. et al. High-performance deep ultraviolet photodetector based on a one-dimensional lead-free halide perovskite CsCu_2I_3 film with high stability. *J. Phys. Chem. Lett.* **11**, 6880–6886 (2020).
143. Li, T. et al. Antisolvent-processed one-dimensional ternary rubidium copper bromine microwires for sensitive and flexible ultraviolet photodetectors. *ACS Appl. Mater. Interfaces* **13**, 49007–49016 (2021).
144. Liu, T., Tang, W., Luong, S. & Fenwick, O. High charge carrier mobility in solution processed one-dimensional lead halide perovskite single crystals and their application as photodetectors. *Nanoscale* **12**, 9688–9695 (2020).
145. Zhang, Y., Liu, F., Jiang, C., Tang, F. & Zhang, X. A perovskite single crystal with one-dimensional structure enables photodetection with negligible hysteresis. *J. Mater. Chem. C* **9**, 3470–3476 (2021).
146. Chen, C. et al. Circularly polarized light detection using chiral hybrid perovskite. *Nat. Commun.* **10**, 1927 (2019).
147. Ishii, A. & Miyasaka, T. Direct detection of circular polarized light in helical 1D perovskite-based photodiode. *Sci. Adv.* **6**, eabd3274 (2020).
148. Zhao, Y. et al. Chiral 1D perovskite microwire arrays for circularly polarized light detection. *Giant* **9**, 100086 (2022).
149. Yang, B. et al. Lead-free halide Rb_2CuBr_3 as sensitive x-ray scintillator. *Adv. Mater.* **31**, 1904711 (2019).
150. Gao, W. et al. One-dimensional all-inorganic K_2CuBr_3 with violet emission as efficient x-ray scintillators. *ACS Appl. Electron. Mater.* **2**, 2242–2249 (2020).
151. Zhang, Z. et al. Lead-free bright yellow emissive Rb_2AgCl_3 scintillators with nanosecond radioluminescence. *J. Lumin.* **241**, 118500 (2022).
152. Yang, J.-M. et al. 1D hexagonal $\text{HC}(\text{NH}_2)_2\text{PbI}_3$ for multilevel resistive switching nonvolatile memory. *Adv. Electron. Mater.* **4**, 1800190 (2018).
153. Song, X. et al. One-dimensional $(\text{NH}=\text{CINH}_2)_3\text{PbI}_5$ perovskite for ultralow power consumption resistive memory. *Research* **2021**, 9760729 (2021).
154. Creason, T. D. et al. Rb_2CuX_3 ($X = \text{Cl}, \text{Br}$): 1D all-inorganic copper halides with ultrabright blue emission and up-conversion photoluminescence. *Adv. Opt. Mater.* **8**, 1901338 (2019).
155. Guan, X. et al. Low-dimensional metal-halide perovskites as high-performance materials for memory applications. *Small* **18**, 2203311 (2022).